AGU PUBLICATIONS

JGR

Journal of Geophysical Research: Space Physics

RESEARCH ARTICLE

10.1002/2015JA021149

Key Points:
- First multifluid MHD simulation of Europa's plasma interaction presented
- Matches plasma and magnetic field observations during Galileo E4 and E26 flybys
- Plasma flow and temperatures different for magnetospheric and pick up ions

Correspondence to:
M. Rubin,
martin.rubin@space.unibe.ch

Citation:
Rubin, M., et al. (2015), Self-consistent multifluid MHD simulations of Europa's exospheric interaction with Jupiter's magnetosphere, *J. Geophys. Res. Space Physics*, *120*, 3503–3524, doi:10.1002/2015JA021149.

Received 21 FEB 2015
Accepted 7 APR 2015
Accepted article online 10 APR 2015
Published online 12 MAY 2015
Corrected 5 OCT 2015

This article was corrected on 5 OCT 2015. See the end of the full text for details.

Self-consistent multifluid MHD simulations of Europa's exospheric interaction with Jupiter's magnetosphere

M. Rubin[1], X. Jia[2], K. Altwegg[1], M. R. Combi[2], L. K. S. Daldorff[2], T. I. Gombosi[2], K. Khurana[3], M. G. Kivelson[2,3], V. M. Tenishev[2], G. Tóth[2], B. van der Holst[2], and P. Wurz[1]

[1]Physikalisches Institut, University of Bern, Bern, Switzerland, [2]Atmospheric, Oceanic and Space Sciences, University of Michigan, Ann Arbor, Michigan, USA, [3]Earth, Planetary and Space Sciences, University of California, Los Angeles, California, USA

Abstract The Jovian moon, Europa, hosts a thin neutral gas atmosphere, which is tightly coupled to Jupiter's magnetosphere. Magnetospheric ions impacting the surface sputter off neutral atoms, which, upon ionization, carry currents that modify the magnetic field around the moon. The magnetic field in the plasma is also affected by Europa's induced magnetic field. In this paper we investigate the environment of Europa using our multifluid MHD model and focus on the effects introduced by both the magnetospheric and the pickup ion populations. The model self-consistently derives the electron temperature that governs the electron impact ionization process, which is the major source of ionization in this environment. The resulting magnetic field is compared to measurements performed by the Galileo magnetometer, the bulk properties of the modeled thermal plasma population is compared to the Galileo Plasma Subsystem observations, and the modeled surface precipitation fluxes are compared to Galileo Ultraviolet Spectrometer observations. The model shows good agreement with the measured magnetic field and reproduces the basic features of the plasma interaction observed at the moon for both the E4 and the E26 flybys of the Galileo spacecraft. The simulation also produces perturbations asymmetric about the flow direction that account for observed asymmetries.

1. Introduction

The interaction between the moons of Jupiter and its magnetosphere has been the subject of various studies during the last three decades. Europa hosts a thin neutral gas atmosphere, which is tightly coupled to Jupiter's magnetosphere. Magnetospheric ions impacting the surface sputter off neutral atoms and molecules. Upon ionization, these particles drive currents that, along with Europa's induced magnetic field, modify the magnetic field near the moon.

Both theoretical and numerical analyses have been performed to understand the plasma and field environment of Europa. The neutral atmosphere has been modeled with a Monte Carlo technique by, e.g., *Shematovich et al.* [2005], *Smyth and Marconi* [2006], *Cassidy et al.* [2007, 2008, 2009], and *Plainaki et al.* [2010, 2012]. MHD simulations of Europa's plasma interaction were performed by, e.g., *Kabin et al.* [1999], *Liu et al.* [2000], *Saur et al.* [1998], and *Schilling et al.* [2008]. The interaction of the Jovian magnetosphere with Europa has further been studied by *Wolff and Mendis* [1983], *Schreier et al.* [1993], *Johnson et al.* [1998], *Volwerk et al.* [2001], *Paranicas et al.* [1998], *Cooper et al.* [2001], *Ip* [1996], *Ip et al.* [1998], and *Kivelson et al.* [1999]. *Lipatov et al.* [2010] used a hybrid kinetic model to simulate the magnetospheric interaction [see also *Lipatov and Combi*, 2006]. Ion fluxes impinging on the surface were modeled by, e.g., *Pospieszalska and Johnson* [1989] and recently by *Truscott et al.* [2011].

Here we use our multifluid MHD model to study the interaction of Jupiter's magnetospheric plasma with Europa's neutral and plasma environment. Multifluid MHD reproduces some of the basic features otherwise only accessible to kinetic approaches that track individual ions in the **E** and **B** fields. A new aspect of the present work is that it separates the dynamics of the different ion populations, i.e., the magnetospheric and pickup ion populations in a fluid model. Furthermore, we improved the calculation of the electron temperature, which we include in the computation of the electron impact ionization rate and electron heat conduction along the magnetic field lines. Compared with kinetic approaches, the computational cost of a multifluid simulation is significantly lower, which in turn allows us to resolve the thermal distribution of Europa's neutral atmosphere with short-scale lengths of a few tens of kilometers

above the surface. It should be made clear, however, that details of the particles' velocity distribution function and kinetic nature still require adaptive hybrid or fluid/kinetic approaches with a nonuniform mesh.

Our simulation uses as input properties of particles and fields near Europa. In the following subsections, we review relevant properties of Europa and its magnetospheric environment. Section 2 describes the model and input parameters. Section 3 addresses some numerical details of the model. Section 4 summarizes the results. Section 5 reviews our main findings that are found largely to be in good accord with observations.

1.1. Europa's Ionosphere

Jupiter's moon Europa is surrounded by a thin surface-bound neutral exosphere. The neutral species in Europa's atmosphere are mostly provided by ion sputtering of the water ice surface. Energetic ions and electrons from the Jovian magnetosphere produce molecular oxygen O_2, the dominant species in Europa's atmosphere, by radiolytic decomposition of water ice [*Johnson*, 1990] and will be discussed in the next section.

Very close to the moon's surface, the probability for collisional interaction between the gaseous species is close to the limit for a surface-bound exosphere [*Hall et al*., 1995; *McGrath et al*., 2004]. *Hall et al*. [1995] used the Goddard High-Resolution Spectrograph of the Hubble Space Telescope to observe the Oxygen I atomic emissions 1304 Å and 1356 Å in the exosphere to derive a molecular oxygen column density of $(1.5 \pm 0.5) \cdot 10^{19}$ m^{-2}. The observed atomic oxygen emission line intensity ratios were interpreted as evidence of the electron impact dissociation of O_2 as the dominant excitation mechanism. These results are consistent with later ultraviolet measurements taken by *Hall et al*. [1998] and Cassini Ultraviolet Imaging Spectrograph (UVIS) observations by *Hansen et al*. [2005]. *Saur et al*. [2011] report a lower limit of the O_2 column density of 10^{18} m^{-2} on the leading side of Europa derived from the Hubble Space Telescope campaign on 29 June 2008. Further observations and models thereof have been presented by *Cassidy et al*. [2008]. An extended sodium atmosphere was detected with a ground-based telescope by *Brown and Hill* [1996]. Impacting ions and electrons are responsible for the sputtered atoms and molecules in Europa's atmosphere and solar heat flux accounts for the water sublimation at the subsolar point. Recently, a transient water plume, possibly tied to tidal stresses on Europa's surface, has been detected [*Roth et al*., 2014], implying an additional, localized source of neutrals. Some of the observed, less abundant species in the atmosphere of Europa originate from implantation of magnetospheric ions, such as sulfur, into the ice matrix on the surface or through the decomposition of hydrated minerals from a possible subsurface ocean or exposed from the ice layer [*Cooper et al*., 2001].

Neutral particles can also be released thermally. The temperature of the surface has been determined by *Spencer et al*. [1999] from measurements of the thermal radiation with the PhotoPolarimeter-Radiometer on the Galileo spacecraft. Because of the low surface temperature ($T \leq 120$ K), the ice sublimation rate is very low at Europa and the corresponding scale height of the thermal population is of the order of only a few tens of kilometers.

The main loss mechanisms for neutral atmospheric particles are electron impact ionization [*Saur et al*., 1998], photoionization, as well as escape when neutral particles leave Europa's Hill sphere at roughly 8.7 Europa radii. The ionization produces an ionosphere around Europa and also an ion tail of new exospheric molecular ions. This ionosphere has been observed during five (of six) radio occultations performed by the Galileo spacecraft [*Kliore et al*., 1997]. The measurements revealed a maximum electron density of nearly 10^4 per cubic centimeter near the surface. Further away, the electron energy distribution at Europa's orbital distance has been presented by *Paranicas et al*. [2001].

1.2. Irradiation and Sputtering Processes on Europa's Surface

The Galilean satellites are subject to continuous irradiation by ions and electrons [*Paranicas et al*., 2009; *Kivelson et al*., 2009]. The collisional impact of the magnetospheric ions is the main source for Europa's tenuous, gravitationally bound atmosphere [*Saur et al*., 1998]. The ions originate from the solar wind and from volcanic release on Jupiter's moon Io. The latter form a neutral gas and plasma torus in the vicinity of the orbit of Io. Upon ionization they are picked-up by the Jovian magnetosphere, accelerated, and ultimately some of these ions hit Europa, which orbits just outside of Io's plasma torus at a radial distance of about 9 Jovan radii. Furthermore, neutral atoms and molecules in Europa's exosphere can be ionized and then impact the moon again.

According to *Bagenal* [1994] the total number density of thermal ions at the centrifugal equatorial plane near Europa's orbit is on the order of $n_i \approx 80\,cm^{-3}$ with a composition of 50% O^+, 25% O^{++}, and 8% each S^{++} and

S^{+++}. Bulk corotating ions, electrons, and pickup ions with small gyroradii first impact the trailing hemisphere, whereas the faster and more energetic ions including those of solar wind origin are more uniformly distributed as shown by the Galileo Energetic Particle Detector (EPD) experiment [*Williams et al*., 1992].

Measured and modeled sputtering yields by impacting O^+, S^+, and H^+ on water ice are strongly depending on the impactor energy, ice temperature, and atomic number and have been presented by *Shi et al*. [1995], *Famá et al*. [2008], and *Cassidy et al*. [2010] [cf. *Johnson*, 1989]. The surface erosion effect of sputtering is probably not spatially uniform [*Ip et al*., 1998]. The directional sputtering by the thermal atomic oxygen and sulfur ions and the exospheric pickup of the molecular oxygen ions can locally enhance surface erosion. Also, the implantation of sulfur ions into the ice surface seems to be enhanced on the trailing hemisphere, consistent with the observations of SO_2 on Europa's surface by the International Ultraviolet Explorer [*Lane et al*., 1981] and the Hubble Space Telescope [*Noll et al*., 1995]. This nonuniform distribution is also supported by the recent work by *Hendrix et al*. [2011] who used high-resolution observations of the SO_2 absorption band from the Galileo Ultraviolet Spectrometer.

Energetic electrons (and their bremsstrahlung) are responsible for the radiolysis taking place within the first meter of the surface [*Paranicas et al*., 2002]. O_2 and H_2 are formed in the surface ice through radiolytic decomposition of water by the impinging electrons as well as the ions. Given their small gyroradii, these electrons impact predominantly the trailing hemisphere as shown by *Paranicas et al*. [2001] who used measurements from Galileo's Near-Infrared Mapping Spectrometer to compare Europa's hydrate distribution (possibly radiolytically produced sulfuric acid hydrates) to the distribution of surface impinging electrons. *Paranicas et al*. [2001] also present energy spectra of these electrons from the Galileo EPD and Voyager 1 Low-Energy Charged Particle Experiment instruments.

1.3. Magnetic Field Perturbations in the Vicinity of Europa

Clear evidence of moon-magnetosphere interaction is found in the measured magnetic field perturbations presented in *Kivelson et al*. [1999, 2009]. The interaction is dominated by the perturbations associated with the presence of an Alfvén wing [*Neubauer*, 1998] and additional contributions from an induced dipole moment [*Kivelson et al*., 1997]. Fits of dipole field models to these measurements are consistent with an induced dipole field with surface strength, $B_{\text{equatorial}} < 120$ nT, which is smaller than the ambient Jovian magnetic field $B_{\text{Jovian}} \sim 450$ nT, but on the order of the time-varying component of the Jovian magnetic field at Europa [*Kivelson et al*., 1997]. A recent study by *Khurana et al*. [2011] gives evidence of electromagnetic induction also at Io but the induced current at Io flows in a global conducting magma ocean, whereas the induced current at Europa flows in a putative subsurface water ocean. Therefore, two separate current systems can form that close either through the conductive interior or through the permanently bound ionosphere and thereby alter the electric and magnetic field topology around Europa, and in the latter case, by formation of a pair of Alfvén wings [*Neubauer*, 1998, 1999].

Ions created in the atmosphere perform cycloidal motions in the local electric and magnetic fields on a spatial scale that displaces their gyrocenters away from their source location, whereas the new electrons, given their small gyroradii, are only marginally displaced from to the magnetic field line on which they are created. This charge separation produces a pickup current channeled to the Jovian ionosphere by a pair of field-aligned currents of the sort observed at Io by Voyager 1 [*Ness et al*., 1979] and at the other Galilean moons including Europa [*Kivelson et al*., 2009]. This effect further alters the electric and magnetic field topology around Europa.

The influence of the induced dipole on the Alfvén current system is further discussed in, e.g., *Volwerk et al*. [2007], *Schilling et al*. [2008], and *Zimmer et al*. [2000]. When Galileo flew by the moon in 1996, picked-up ions from the ionosphere were detected by the plasma instrument [*Paterson et al*., 1999] and clear marks of the mass loading process, in addition to an induced magnetic field, have been observed by the Galileo magnetometer [*Kivelson et al*., 2009].

2. Model Description

The simulation model is based on the Block-Adaptive Tree Solar wind Roe-type Upwind Scheme (BATS-R-US) component of the Space Weather Modeling Framework described in more detail in *Powell et al*. [1999] and *Tóth et al*. [2005, 2012]. The multifluid model has also been successfully used in the case of comets [*Rubin*

Table 1. Model Species With Dominant Production and Loss Processes

Name	Major Production Process	Major Loss Process
O^+ magnetospheric and pickup ions	$O_2 + e^- \rightarrow O^+ + O + 2e^-$	$O^+ + e^- \rightarrow O$
O_2^+ pickup ions	$O_2 + e^- \rightarrow O_2^+ + 2e^-$	$O_2^+ + e^- \rightarrow O_2$ and $O_2^+ + e^- \rightarrow O + O$
Electrons	$O_2 + e^- \rightarrow O_2^+ + 2e^-$	$O_2^+ + e^- \rightarrow O_2$ and $O_2^+ + e^- \rightarrow O + O$

et al., 2014a], Earth [*Glocer et al*., 2009], and Mars [*Najib et al*., 2011]. First, we discuss the model parameters and the choice of model species, and then we discuss the model equations that are solved and how we adapted them to Europa.

2.1. Model Input Parameters

We analyze the environment of Europa using a multifluid magnetohydrodynamic (MHD) model. As a result of Jupiter's sidereal rotation period of about 10 h and the tilt of the dipole by approximately 10° the plasma and magnetic field environment at the location of Europa is continually changing. Therefore, the simulation results are snapshots for the time of the E4 and E26 flybys. Table 1 summarizes the included plasma populations. Furthermore, it shows their corresponding dominant source and loss processes, although these can change with location. Ion-electron recombination is generally of minor importance; the major loss inside the domain is impact on the surface of Europa. The first fluid consists of the oxygen ions, mostly magnetospheric oxygen and some contribution of picked-up oxygen from dissociative electron impact ionization. The second fluid represents the molecular oxygen pickup ions originating from mass loading through electron impact ionization, photoionization, and charge exchange with the neutral exosphere. The third component represents the electrons, treated as a charge-neutralizing fluid. In this first approach we assume that the charge state of the involved species is unity. In the future we plan to include protons and also magnetospheric ions at higher charge state.

The magnetospheric oxygen ions are injected into the system at the upstream boundary of the simulation domain. The loss processes included in our model are charge exchange with Europa's neutral gas and ion-electron recombination. In the close vicinity of the moon these ions are also coupled to the other neutral and plasma species through elastic collisions by which they transfer momentum. Given the low collision rates, however, the coupling is rather limited. Our equations do not treat the magnetospheric ion population and the pickup ion population separately. Instead, we treat all ions of the same mass and charge as a single fluid independent of their source. The plasma around Europa, however, is dominated by molecular oxygen ions, O_2^+, and mostly produced by electron impact ionization of the neutral gas. A basic assumption of our approach is that the plasma is charge neutral, so the charge density of electrons is consistent with the total charge density of the ions.

Paranicas et al. [2009] provide the energy spectra of the upstream ions measured by the Energetic Particle Detector experiment on the Galileo orbiter [cf. *Paranicas et al*., 2002]. Sampling times and locations were chosen to avoid the region of direct satellite sweeping to obtain a representative upstream environment. On the basis of these results and the magnetic field observations [*Khurana et al*., 2009; *Kivelson et al*., 1999] we have chosen the upstream plasma parameters shown in Table 2 as boundary conditions for our simulations.

The model includes a magnetic dipole field arising from induced currents inside Europa's conducting water ocean due to the time-varying external field. For this we assume that the moon is a highly conductive sphere with Europa's radius. In such a case, induced currents produce a dipole whose polar field at the surface of the sphere precisely cancels the instantaneous time-varying B field components of the background field [*Kivelson et al*., 1999]. We furthermore assume that the external B_z component diffused through the moon, i.e., by ignoring small periodic variations of B_z, and the induced magnetic field opposes the change of the B_x and B_y components of the external field. The induced dipole field is fixed for the time of the closest approach. The strength and orientation of the induced dipole for the two flybys can be found in Table 2.

2.1.1. Model Equations

In this section we start with a general discussion of the applied multifluid equations, and we adapt the equations to Europa later. The multifluid equations include the ion continuity equation

$$\frac{\partial \rho_s}{\partial t} + \nabla \cdot (\rho_s \boldsymbol{u}_s) = \frac{\delta \rho_s}{\delta t} \tag{1}$$

Table 2. Boundary Conditions for the E4 and E26 Flybys [*Kivelson et al.*, 1999, 2009][a]

	E4	E26
Closest approach (CA)	19-Dec-1999 06:52:58 UTC	03-Jan-2000 17:59:43 UTC
CA EPhiO$_x$	0.84 R_E	−0.83 R_E
CA EPhiO$_y$	1.17 R_E	0.08 R_E
CA EPhiO$_z$	−0.03 R_E	−0.89 R_E
CA distance from center	1.45 R_E	1.22 R_E
Magnetospheric plasma bulk velocity u_x component	100 km/s	100 km/s
Magnetospheric plasma bulk velocity u_y component	0 km/s	0 km/s
Magnetospheric plasma bulk velocity u_z component	0 km/s	0 km/s
Magnetospheric plasma density	20 cm^{-3}	20 cm^{-3}
Magnetospheric electron temperature	$1.5 \cdot 10^6$ K	$1.5 \cdot 10^6$ K
Magnetospheric O^+ temperature	$1.5 \cdot 10^6$ K	$1.5 \cdot 10^6$ K
Jovian magnetic field B_x component	55 nT	−22 nT
Jovian magnetic field B_y component	−173 nT	205 nT
Jovian magnetic field B_z component	−412 nT	−379 nT
Europa's induced magnetic field dipole strength	92 nT	103 nT
Europa's induced magnetic field dipole longitude	17° East	174° West
Europa's induced magnetic field dipole latitude	0°	0°

[a]By convention, the origin of longitude is at the Jupiter-facing meridian plane (cf. Figure 6).

with ρ_s and $\boldsymbol{u}_s$ the mass density and center of mass velocity for ion species s. The right-hand side contains the source and loss terms ($\delta\rho_s/\delta t$) and will be discussed later on. The momentum equation

$$\frac{\partial(\rho_s \boldsymbol{u}_s)}{\partial t} + \nabla \cdot (\rho_s \boldsymbol{u}_s \boldsymbol{u}_s + \boldsymbol{I} p_s) - Z_s e \frac{\rho_s}{m_s}(\boldsymbol{E} + \boldsymbol{u}_s \times \boldsymbol{B}) - \rho_s \boldsymbol{g} = \frac{\delta(\rho_s \boldsymbol{u}_s)}{\delta t} \tag{2}$$

with the identity matrix $\boldsymbol{I}$ implying isotropic pressure, $\boldsymbol{g}$ the gravitational acceleration vector, and m_s, p_s, and Z_s the mass, pressure, and charge state of ion species s, respectively. It includes finite ion gyroradii effects due to the difference in the bulk velocities (but not the thermal velocities) of the fluids. The right-hand side ($\delta(\rho_s \boldsymbol{u}_s)/\delta t$) are the source and loss terms. The electric field can be obtained from the generalized Ohm's law:

$$\boldsymbol{E} = -\boldsymbol{u}_e \times \boldsymbol{B} - \frac{1}{n_e e}\nabla p_e + \eta \boldsymbol{j} \tag{3}$$

where $\boldsymbol{j}$ stands for the electric current density derived from Ampère's law and η is the resistivity, respectively. Therefore, a force is exerted on fluids with a velocity difference with respect to the electron velocity (term proportional to $(\boldsymbol{u}_s - \boldsymbol{u}_e) \times \boldsymbol{B}$), hereafter called drift gyration term. The definition of $\boldsymbol{u}_e$ follows below.

The electron number density, assuming charge neutrality, satisfies

$$n_e = \sum_{s=\text{ions}} Z_s n_s \tag{4}$$

and is used to calculate the average velocity of the positive current carriers which differs from the mass-averaged velocities

$$\boldsymbol{u}_+ = \frac{\sum_{s=\text{ions}} Z_s n_s \boldsymbol{u}_s}{n_e} \tag{5}$$

from which we calculate the electron velocity, $\boldsymbol{u}_e$:

$$\boldsymbol{u}_e = \boldsymbol{u}_+ + \boldsymbol{u}_H = \boldsymbol{u}_+ - \frac{\boldsymbol{j}}{n_e e} \tag{6}$$

The Hall velocity, $\boldsymbol{u}_H = -\boldsymbol{j}/n_e e$, in equation (6) serves as a source for whistler waves and describes the velocity difference between the positive and negative charge carriers. It is derived from the net electric current density

$$\boldsymbol{j} = \sum_{s=\text{ions}} Z_s e n_s \boldsymbol{u}_s - n_e e \boldsymbol{u}_e \tag{7}$$

The pressure equation for the individual fluids is

$$\frac{\partial p_s}{\partial t} + (\boldsymbol{u}_s \cdot \nabla) p_s + \gamma p_s (\nabla \cdot \boldsymbol{u}_s) = \frac{\delta p_s}{\delta t} \tag{8}$$

with γ the adiabatic index and $\delta p_s/\delta t$ are the source and loss terms. The electron pressure equation is given by

$$\frac{\partial p_e}{\partial t} + (\boldsymbol{u}_e \cdot \nabla) p_e + \gamma p_e (\nabla \cdot \boldsymbol{u}_e) + (\gamma - 1) \nabla \cdot \boldsymbol{h}_e|_{\parallel \boldsymbol{B}} = \frac{\delta p_e}{\delta t} \tag{9}$$

with p_e the electron pressure and $\boldsymbol{h}_e|_{\parallel \boldsymbol{B}}$ the field-aligned electron heat flow vector and $\delta p_e/\delta t$ stands for the source and loss terms. In our current approach we use a single electron pressure equation and do not distinguish between the electron populations of magnetospheric and electron impact (pickup) origin. The right-hand sides of equations (8) and (9) are the source terms to be discussed in the next section.

Faraday's law of induction is

$$\frac{\partial \boldsymbol{B}}{\partial t} = -\nabla \times \boldsymbol{E} \tag{10}$$

Using equations (3) and (6) the magnetic induction equation can be written in the form [cf. *Ma et al.*, 2007]

$$\frac{\partial \boldsymbol{B}}{\partial t} = \nabla \times \left(\boldsymbol{u}_+ \times \boldsymbol{B} - \frac{\boldsymbol{j}}{n_e e} \times \boldsymbol{B} + \frac{1}{n_e e} \nabla p_e - \eta \boldsymbol{j} \right) \tag{11}$$

The terms on the right side of the equation are the convection term, the Hall term, the electron pressure gradient term, and the resistivity term. Given the high computational cost of solving for whistler waves, we did not include the Hall term. Accordingly, in equation (6) we used $\boldsymbol{u}_e = \boldsymbol{u}_+$ with $\boldsymbol{u}_H = 0$ but accounted for the different bulk speeds of ions and electrons in the source terms discussed in section 2.4.

2.2. Resistivity

We include in Ohm's law (equation (3) cf. equation (10)) the effect of resistivity due to collisions of electrons with neutrals and ions. The resistivity, η, is calculated from

$$\eta = \frac{1}{\sigma_e} = \frac{1}{\sigma_{en}} + \frac{1}{\sigma_{ei}} \tag{12}$$

with σ_e the electron conductivity, which is derived from the collision rates of the electrons with neutrals and ions:

$$\begin{aligned} \sigma_{en} &= \frac{e^2 n_e}{\sum_{n'=\text{neutrals}} \overline{\nu}_{en'} m_e} \\ \sigma_{ei} &= \frac{e^2 n_e}{\sum_{s'=ions} \overline{\nu}_{es'} m_e} \end{aligned} \tag{13}$$

The individual rates for the corresponding species will follow later in this paper.

2.3. Electron Heat Conduction

Electron impact ionization is the major ionization process in Europa's environment [*Saur et al.*, 1998] and, as will be discussed later, the electron temperature and ionization rate are tightly coupled. Electrons can transport heat along the magnetic field line they are tied to and thus, as described by *van der Holst et al.* [2011], we separately solve the electron internal energy density E_e accounting for the thermal electron heat flux with heat conductivity, C_e:

$$\frac{\partial E_e}{\partial t} + \nabla \cdot (E_e \boldsymbol{u}_e) + p_e \nabla \cdot \boldsymbol{u}_e = \nabla \cdot \boldsymbol{h}_e|_{\parallel \boldsymbol{B}} = \nabla \cdot \left(C_e \nabla T_e|_{\parallel \boldsymbol{B}} \right) \tag{14}$$

The value for C_e (in $\mathrm{W\,m^{-1}\,K^{-1}}$) is tied to the resistivity of the electrons discussed above, i.e., inversely proportional to the resistivity, η, from equation (12), and is given by

$$C_e = \frac{T_e}{\eta} \left(\frac{k_B}{e} \right)^2 \tag{15}$$

An upper limit to the free-streaming heat flux is related to the thermal velocity, v_{th}, of the electrons and the associated heat transport: $F_e^{\text{free}} = n_e v_{\text{th}} k_B T_e$, but most likely the maximum heat transport is much smaller and we apply the following formulation for the heat flux:

$$\boldsymbol{h}_e = -\min \left(C_e, \frac{f F_e^{\text{free}}}{|\nabla T_e|} \right) \nabla T_e \tag{16}$$

with f the flux limiter, which is an input parameter of the model and has been set to 5%. This approach limits the maximum heat flux in regions with large gradients in the electron temperature and limited collisions to

physically realistic values. We furthermore require the thermal heat conduction vector to be aligned with the magnetic field, accounting for the fact that most electrons have small gyroradii:

$$\boldsymbol{h}_e\big|_{\|\boldsymbol{B}} = \frac{\boldsymbol{h}_e \cdot \boldsymbol{B}}{|\boldsymbol{B}|^2}\boldsymbol{B} \tag{17}$$

which corresponds to the projection of the heat flux vector onto the magnetic field.

2.4. Source Terms

The source terms contain much of the physics describing the mass loading and the collisional interactions between the involved species. The source term $\frac{\delta\rho_s}{\delta t}$ on the right-hand side of the continuity equation (equation (1)) contains the sources and losses of the plasma mass density

$$\begin{aligned}\frac{\delta\rho_s}{\delta t} = {} & m_s \sum_{n=\text{neutrals}} \nu^{io}_{n\to s} n_n \\ & - m_s \sum_{\substack{n,\ n' = \text{neutrals} \\ s' = \text{ions}}} n_n n_s k_{ns\to n's'} \\ & + m_s \sum_{\substack{n,\ n' = \text{neutrals} \\ s' = \text{ions}}} n_n n_{s'} k_{ns'\to n's} \\ & - m_s \alpha_s n_e n_s\end{aligned} \tag{18}$$

The first term stands for contributions to the mass density from ionization of neutrals ($\nu^{io}_{n\to s}$ combined electron impact and photo ionization rate and n_n the corresponding neutral gas number density). Terms two and three are loss and additions through charge exchange (rate $k_{ns\to n's'}$ removes an ion of species s and a neutral n and forms an ion and neutral of species n' and s'). In our general description terms two and three loop through all ion-neutral combinations in $k_{ns\to n's'}$ and $k_{ns'\to n's}$, respectively. However, since only resonant charge exchange is considered in this work, most of these elements are zero. The last term accounts for the loss of ions by ion-electron recombination of species s denoted by α_s.

The source term for the momentum equation (equation (2))

$$\begin{aligned}\frac{\delta(\rho_s \boldsymbol{u}_s)}{\delta t} = {} & m_s \sum_{n=\text{neutrals}} \nu^{io}_{n\to s} n_n (\boldsymbol{u}_n - \boldsymbol{u}_s) \\ & + m_s \sum_{\substack{n,\ n' = \text{neutrals} \\ s' = \text{ions}}} n_n n_{s'} k_{ns'\to n's} (\boldsymbol{u}_n - \boldsymbol{u}_s) \\ & - m_s \bar{\nu}_{se} n_s (\boldsymbol{u}_s - \boldsymbol{u}_e) \\ & + m_s n_s \sum_{s'=\text{ions}} \bar{\nu}_{ss'} (\boldsymbol{u}_{s'} - \boldsymbol{u}_s) \\ & + m_s n_s \sum_{n'=\text{neutrals}} \bar{\nu}_{sn'} (\boldsymbol{u}_{n'} - \boldsymbol{u}_s) \\ & + \frac{\delta\rho_s}{\delta t}\boldsymbol{u}_s\end{aligned} \tag{19}$$

The losses and sources for the momentum equation contain the newly added ions in the first term, the addition through charge exchange in the second, and the terms three through five for the elastic momentum transfer collisions between the ions and electrons (rate $\bar{\nu}_{se}$), other ions ($\bar{\nu}_{ss'}$), and the neutrals ($\bar{\nu}_{sn'}$), respectively. The last term is obtained from the sources and losses of the continuity equation (equation (18)).

For the pressure of ion species s the source terms are

$$\begin{aligned}\frac{\delta p_s}{\delta t} = & -p_s \sum_{\substack{n,\ n' = \text{neutrals} \\ s' = \text{ions}}} n_n n_s k_{ns\to n's'} \\ & - p_s \alpha_s n_e \\ & + 2\sum_{s'=\text{ions}} \overline{\nu}_{ss'} \frac{m_s}{m_{s'} + m_s} n_s k_B (T_{s'} - T_s) \\ & + \frac{2}{3}\sum_{s'=\text{ions}} \overline{\nu}_{ss'} \frac{m_s m_{s'}}{m_{s'} + m_s} n_s (\boldsymbol{u}_{s'} - \boldsymbol{u}_s)^2 \\ & + 2\sum_{n'=\text{neutrals}} \overline{\nu}_{sn'} \frac{m_s}{m_{n'} + m_s} n_s k_B (T_{n'} - T_s) \\ & + \frac{2}{3}\sum_{n'=neutrals} \overline{\nu}_{sn'} \frac{m_{n'} m_s}{m_{n'} + m_s} n_s (\boldsymbol{u}_{n'} - \boldsymbol{u}_s)^2 \\ & + 2\overline{\nu}_{se} n_s k_B (T_e - T_s) \\ & + \frac{2}{3}\overline{\nu}_{se} m_e n_s (\boldsymbol{u}_e - \boldsymbol{u}_s)^2 \\ & + \frac{1}{3} m_s \sum_{n=\text{neutrals}} \nu^{\text{io}}_{n\to s} n_n (\boldsymbol{u}_n - \boldsymbol{u}_s)^2 \\ & + \frac{1}{3} m_s \sum_{\substack{n,\ n' = \text{neutrals} \\ s' = \text{ions}}} n_n n_{s'} k_{ns'\to n's} (\boldsymbol{u}_n - \boldsymbol{u}_s)^2 \end{aligned} \tag{20}$$

The sources and losses of the ion pressure of a species assume an adiabatic index of $\frac{5}{3}$ and contain, in the first two terms, the pressure decrease due to loss of particles through charge-exchange and ion-electron recombination. Terms three to eight include elastic momentum transfer collisions of the ions with the other ions, neutrals, and electrons, respectively, and depend on the involved particle masses. These tend to equilibrate the bulk motions and temperatures of the corresponding ions, neutrals, and electrons. The last two terms increase the pressure through newly added ions by ionization and charge exchange.

The source terms for the electron pressure equation (equation (9)) are

$$\begin{aligned}\frac{\delta p_e}{\delta t} = & -p_e n_e \sum_{s=\text{ions}} \alpha_s n_s \\ & + \frac{1}{3} m_e \sum_{\substack{n = \text{neutrals} \\ \text{s} = \text{ions}}} \nu^{\text{io}}_{n\to s} n_n (\boldsymbol{u}_n - \boldsymbol{u}_e)^2 \\ & + \frac{2}{3}\left(\sum_{\substack{n = \text{neutrals} \\ s = \text{ions}}} \nu^{\text{io,ph}}_{n\to s} n_n Q^{\text{exc}}_{n\to s} - \sum_{\substack{n = \text{neutrals} \\ \text{s} = \text{ions}}} n_e \nu^{\text{io},e}_{n\to s} n_n Q^{\text{pot}}_{n\to s} \right) \\ & + 2\sum_{s'=\text{ions}} \overline{\nu}_{es'} \frac{m_e}{m_{s'}} n_e k_B (T_{s'} - T_e) \\ & + \frac{2}{3}\sum_{s'=\text{ions}} \overline{\nu}_{es'} m_e n_e (\boldsymbol{u}_{s'} - \boldsymbol{u}_e)^2 \\ & + 2\sum_{n'=\text{neutrals}} \overline{\nu}_{en'} \frac{m_e}{m_{n'}} n_e k_B (T_{n'} - T_e) \\ & + \frac{2}{3}\sum_{n'=\text{neutrals}} \overline{\nu}_{en'} m_e n_e (\boldsymbol{u}_{n'} - \boldsymbol{u}_e)^2 \end{aligned} \tag{21}$$

Also, here the pressure is reduced upon ion-electron recombination in the first term. Term two accounts for the newly implanted electrons and the third term accounts for the excess energy of the photoelectrons ($Q^{\text{exc}}_{n\to s}$;

Table 3. Photoionization Excess Energies and Ionization Potentials[a]

Reaction	Electron Energy	Electron Pressure	Reference
$O_2 + h\nu \rightarrow O^+ + O + e^-$	$Q^{exc}_{n\rightarrow s} = 24.0$ eV	source	*Huebner et al.* [1992]
$O_2 + h\nu \rightarrow O_2^+ + e^-$	$Q^{exc}_{n\rightarrow s} = 16.0$ eV	source	*Huebner et al.* [1992]
$O_2 + e^- \rightarrow O^+ + O + 2e^-$	$Q^{pot}_{n\rightarrow s} = 18.8$ eV	sink	estimate
$O_2 + e^- \rightarrow O_2^+ + 2e^-$	$Q^{pot}_{n\rightarrow s} = 12.0$ eV	sink	*Samson and Gardner* [1975]

[a]The estimate of the dissociative electron impact ionization of O_2 is based on the double bond between the oxygen atoms and the ionization potential of atomic oxygen.

increases electron pressure, Table 3) and the ionization energy that has to be provided by the ionizing electron ($Q^{pot}_{n\rightarrow s}$; lowers electron pressure, Table 3). Terms four to seven are again the elastic momentum transfer collisions with the ions and neutrals, respectively. The photoionization frequency $\nu^{io,ph}_{n\rightarrow s}$ and the electron impact ionization rate $\nu^{io,e}_{n\rightarrow s}$ are discussed later on.

2.5. Surface Boundary Conditions

From this section on we describe the part of our model that is specific to Europa. Important for any simulation around a solid object are the surface boundary conditions. We set these such that we allow inflow of plasma to the surface. This is in line with the fact that Europa is constantly bombarded by plasma from Jupiter's magnetosphere. If the flow direction is away from the surface, as for instance in the wake of the satellite, we require the flux to be very small at the surface. This implicitly assumes that there is no net flux of ions out of the surface or that the sputtering process mainly produces neutrals and that the flux of ions is small compared to number of ions in the ionosphere. When investigating minor species this might not be fully true: a few percent of the particles are sputtered off the surface directly as ions.

For the magnetic field we use a floating boundary. This means that the gradient of the magnetic field perturbation (the difference between the total field and the induced dipole field) is set to zero at the moon's surface. Clearly, this is only an approximation for the diffusion processes occurring in the top layers of Europa. While the code is in principle able to solve the diffusion of the magnetic field into the interior of Europa, including layers of different conductance such as the ice crust and a brine water ocean, we defer this aspect of the problem as well as the direct sputtering of ions to our future work.

2.6. Neutral Gas Background

In our model we use a simple analytical description for the neutral molecular oxygen, O_2, atmosphere of the satellite. We use the sum of two exponential functions representing the thermal and the sputtered distributions for the leading and the trailing hemispheres' neutral gas densities, n_L and n_T, respectively:

$$\begin{aligned} n_L &= n_0 \cdot \exp\left(-\frac{|\boldsymbol{r}-\boldsymbol{r_E}|}{H_0}\right) + n_1 \cdot \exp\left(-\frac{|\boldsymbol{r}-\boldsymbol{r_E}|}{H_1}\right) \\ n_T &= n_L \cdot (1 + 2 \cdot \cos(\alpha)) \end{aligned} \tag{22}$$

with H_0 the neutral scale height which is set to 20 km and n_0 the surface density set to $5 \cdot 10^8$ cm^{-3}. The second, more extended sputtered distribution uses $H_1 = 500$ km and $n_1 = 5 \cdot 10^4$ cm^{-3}. Both distributions are in accordance with *Cassidy et al.* [2007]. Furthermore, we assume an enhancement of the neutral density, n_T, centered on the trailing hemisphere due to increased sputtering, which is the dominant source process for the neutral O_2 atmosphere. The angle α on the trailing hemisphere is measured from the undisturbed inflow direction of the magnetospheric plasma and ranges from 0 to 90°. The average column density resulting from integrating this distribution from Europa's surface to infinity is $N_C = 1.6 \cdot 10^{19}\,m^{-2}$ which is in good agreement with the O_2 column density derived from observations $(1.5 \pm 0.5) \cdot 10^{19}$ m^{-2} by *Hall et al.* [1995]. For the neutral gas temperature we use $T = 600$ K and assume the atmosphere to be stationary ($\boldsymbol{u}_n = 0$). Certainly, this neutral atmosphere model is only an approximation and in future applications we plan to couple a more realistic Monte Carlo-type kinetic approach for the neutral exosphere with our MHD model and thereby refine the description of the neutral distribution. Nevertheless, the effect of the neutral gas temperature is only of minor importance given the low densities in Europa's atmosphere and correspondingly the low momentum transfer between the neutral atmosphere and the plasma.

As mentioned in the previous section also the neutral gas environment changes as the magnetospheric conditions vary over the course of one rotation of Jupiter's magnetic field and the moon moves through the magnetospheric current sheet. However, because the model is used in a steady state mode, temporal variations have not been included in our analysis except for the upstream boundary conditions, which are different for the two flybys (Table 2).

2.7. Ionization

Energetic electrons ionize neutral gas in Europa's exosphere. Similar to *Schilling* [2006], we use the ionization rate obtained by integrating the product of the normalized Maxwellian energy distribution, $f_e(E,T_e)$ of the electrons at temperature T_e with the corresponding electron velocity, $v_e(E)$, and electron impact ionization cross section, $\sigma_{n\rightarrow s}(E)$ taken from *Hwang et al.* [1996]

$$\nu_{n\rightarrow s}^{\mathrm{io},e} = \int_{Q_{n\rightarrow s}^{\mathrm{pot}}}^{\infty} f_e(E,T_e)\,\sigma_{n\rightarrow s}(E)\,v_e(E)\,\mathrm{d}E \tag{23}$$

Only electrons with energies higher than the ionization potential, $Q_{n\rightarrow s}^{\mathrm{pot}}$, contribute to the ionization. The Maxwell-Boltzmann energy distribution at temperature T_e is $f_e(E,T_e) = 2\sqrt{\frac{E}{\pi}}\left(\frac{1}{kT_e}\right)^{3/2}\exp\left(\frac{-E}{kT_e}\right)$. For the sake of simplicity we estimated that the branch for the reaction $O_2 + e^- \rightarrow O^+ + O + 2e^-$ amounts to ~ 10% of the reaction $O_2 + e^- \rightarrow O_2^+ + 2e^-$ based on the rates used by *Schreier et al.* [1993] and *Banks and Kockarts* [1973].

A minor source of ionization is photoionization, $\nu_{n\rightarrow s}^{\mathrm{io,ph}}$, for which we apply the frequencies by *Huebner et al.* [1992] scaled to a heliocentric distance of ~ 5.2 AU.

$$\nu_{O_2+h\nu\rightarrow O_2^+ + e^-}^{\mathrm{io,ph}} = 1.70\cdot 10^{-8}\ s^{-1}$$
$$\nu_{O_2+h\nu\rightarrow O^+ + O + e^-}^{\mathrm{io,ph}} = 4.07\cdot 10^{-9}\ s^{-1}$$

These rates are applied everywhere except in the shadow cast by Europa.

2.8. Electron Heating and Cooling

Electrons generated in the photoionization process contribute to the electron pressure while electron impact ionization cools the electrons because the impacting electron has to provide the ionization energy. The energies used in our simulation are listed in Table 2 and then applied to the electron pressure source term (equation (21)).

2.9. (Dissociative) Ion-Electron Recombination

Electrons can recombine with ions, in particular in locations where the electron temperature is low, whereas in regions of high electron temperature the recombination is strongly inhibited. We apply the dissociative electron recombination rate for O_2^+ (given in units of $m^3\,s^{-1}$) from *Schunk and Nagy* [2009]:

$$\alpha_{O_2^+} = 2.4\cdot 10^{-13}\left(\frac{300}{T_e}\right)^{0.7} \tag{24}$$

with T_e the electron temperature. It denotes the total rate summed over all the branching ratios, namely, $O_2^+ + e^- \rightarrow O_2$ and $O_2^+ + e^- \rightarrow O + O$. Also taken from *Schunk and Nagy* [2009] is the rate for recombination of O^+ with electrons (in $m^3\,s^{-1}$):

$$\alpha_{O^+} = 3.7\cdot 10^{-18}\left(\frac{250}{T_e}\right)^{0.7} \tag{25}$$

2.10. Charge Exchange

The model also includes charge exchange interactions between the neutral exosphere and the plasma. In the MHD source terms (equations (18)–(21)) this is included through ion-neutral friction. The rate for the ion-neutral friction of O_2^+ with O_2 is given by *Schunk and Nagy* [2009] (in units of $m^3\ s^{-1}$):

$$k_{O_2,\,O_2^+} = 2.59\cdot 10^{-17} n_{O_2}\sqrt{T_r}(1 - 0.073\cdot \log_{10}T_r)^2 \tag{26}$$

The rate depends on the neutral gas density, n_{O_2}, and the reduced temperature $T_r = \frac{\left(T_{O_2}+T_{O_2^+}\right)}{2}$ while the interaction of O^+ with O_2 is nonresonant and will be treated as an elastic collision discussed in the next section.

2.11. Elastic Collisions

To track exchange of momentum and energy between the different fluids, we use the numerical approximations for the momentum transfer collision frequencies given in *Schunk and Nagy* [2009]:

$$
\begin{aligned}
&O^+ \text{ and } O_2^+ : \bar{\nu}_{st} = 1.27 \cdot 10^{-6} \frac{Z_s^2 Z_t^2 \sqrt{m_{st}}\ n_t}{m_s \quad T_{st}^{3/2}} \\
&O^+ \text{ and } O_2 : \bar{\nu}_{sn} = 10^{-6} C_{sn} n_n \\
&e^- \text{ and } O^+ \text{or } O_2^+ : \bar{\nu}_{es} = 54.5 \cdot 10^{-6} \frac{n_s Z_s^2}{T_e^{3/2}} \\
&O^+ \text{or } O_2^+ \text{ and } e^- : \bar{\nu}_{se} = 1.27 \cdot 10^{-6} \frac{\sqrt{m_e} n_e Z_s^2}{m_s \ T_e^{3/2}} \\
&e^- + O_2 : \bar{\nu}_{en} = 1.82 \cdot 10^{-16} n_n \left(1 + 3.6 \cdot 10^{-2} \sqrt{T_e}\right) \sqrt{T_e}
\end{aligned}
\tag{27}
$$

Z_s and Z_t are the charge states of the ions, m_s is the atomic mass of species s (in amu), m_{st} is the reduced mass (in amu), m_e the electron mass (in amu), n_t and n_s are the number densities of species t and s (in m^{-3}), and n_n is the density of the corresponding neutral, respectively. C_{sn} are numerical coefficients taken from *Schunk and Nagy* [2009]. The reduced mass, m_{st}, and reduced temperature, T_{st}, for the ion-ion interactions are calculated by

$$
\begin{aligned}
m_{st} &= \frac{m_s m_t}{m_s + m_t} \\
T_{st} &= \frac{m_s T_t + m_t T_s}{m_s + m_t}
\end{aligned}
\tag{28}
$$

and depend on the masses and temperatures of the involved species, m_s, m_t, T_s, and T_t (given in amu and K, respectively). The rates contain the collision frequencies depending on the density of the collision partner and they are modified by the masses of the constituent particles to track the momentum exchanged ($\bar{\nu}_{st} \neq \bar{\nu}_{ts}$).

3. Numerical Aspects

The multifluid MHD code BATS-R-US [*Powell et al.*, 1999] described in section 2 uses an adaptive mesh that resolves the different length scales involved in the interaction [*Tóth et al.*, 2012]. The modeled domain size extends along all axes from -32 to $32\,R_E$ (with Europa's radius $R_E \sim 1569$ km). This rectangular simulation domain is discretized with a stretched spherical mesh with the smallest cells of the order of 10 km in the vicinity of the moon growing exponentially to approximately 5000 km at the edge of the domain. The adaptive grid consists of 30,000 grid blocks containing 512 cells each, so in total there are approximately 15 million grid cells. Each block represents a different physical volume, however, in the generalized coordinates used for the computation they all have the same size. The simulation is run in parallel on 256 processors.

The results presented in this paper were obtained with the local Rusanov or total variation diminishing (TVD) Lax-Friedrich scheme [*Rusanov*, 1961] with minmod limiter. We used a local time stepping approach in which each cell is advanced at its locally stable time step [*Tóth et al.*, 2012]. This is used to speed up the convergence toward the steady state solution. To avoid problems associated with the stiffness of the source terms and allow larger local time steps, we use a point-implicit scheme that involves a linear system of equations to be solved independently in each grid cell. The matrix is formed from the partial derivatives of the source terms that are obtained numerically. This is computationally costly but, on the other hand, allows us to significantly increase the numerical time step of the simulation.

For the electron heat conduction calculation (equation (14)) [*van der Holst et al.*, 2014], which depends on spatial derivatives, the point-implicit approach is not applicable. We therefore use a semi-implicit approach. The heat conduction is solved implicitly with the Generalized Minimal Residual (GMRES) Krylov subspace type iterative solver [*Saad and Schultz*, 1986] with a Block Incomplete Lower-Upper decomposition preconditioner as described by *Tóth et al.* [2012].

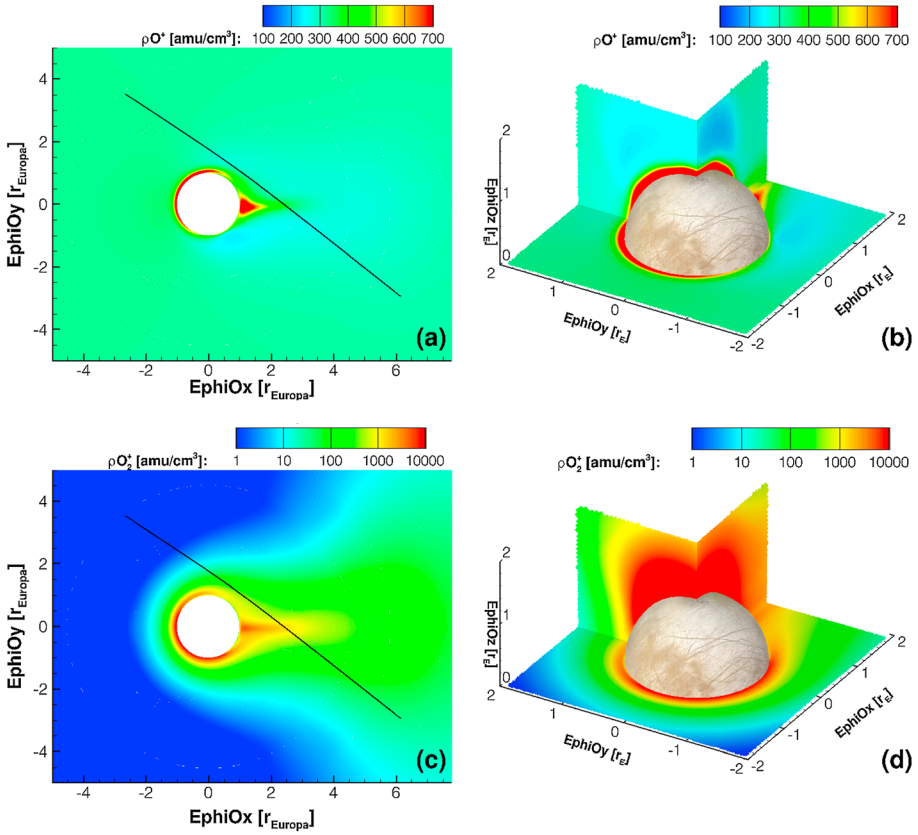

Figure 1. (a) O^+ mass density around Europa for the E4 flyby in EphiO coordinates. The trailing hemisphere facing the inflow of the magnetospheric plasma is on the left-hand side. The black line shows Galileo's trajectory projected onto this plane from roughly 20 min before until 30 min after closest approach. The positive EphiO *y* direction points toward Jupiter. (b) O^+ mass density in the close vicinity of Europa in three perpendicular cuts. (c, d) Same as Figures 1a and 1b but for O_2^+. Both species show an asymmetry about the upstream flow direction.

4. Results and Discussion

Simulations were performed for the plasma conditions encountered during the Galileo E4 and E26 flybys. We have chosen the E4 flyby through the wake to compare our results with the previous simulations by *Kabin et al.* [1999] and *Liu et al.* [2000] using BATS-R-US. The E26 flyby was selected because it is an upstream flyby and occurs under different magnetospheric conditions from E4. The two flybys took place at distinct locations with respect to Jupiter's central plasma sheet; therefore, different upstream boundary conditions were used as indicated in Table 2. The results are displayed in the EphiO coordinate system that is centered at Europa and has its *z* axis parallel to Jupiter's axis of rotation (O stands for Ω) and the *y* axis corresponds to the direction from Europa to Jupiter projected into the plane perpendicular to the *z* axis. The *x* axis along the direction of corotation completes the right-handed system and thus represents the azimuthal direction (phi) with respect to Jupiter. Since we obtain steady state snapshots of the interaction of Europa with the Jovian magnetosphere, we freeze the coordinate system at the time of the closest approach of the Galileo spacecraft with Europa to obtain the inertial system for our simulation. The same treatment has been applied to the magnetometer data [cf. *Kivelson et al.*, 1999].

4.1. Simulation Results for the E4 Flyby

Figure 1 shows the obtained plasma distribution around Europa in EphiO coordinates. Figure 1a shows the mass density of O^+ ions of magnetospheric origin with a contribution of pickup ions from dissociative electron impact ionization through the channel $O_2 + e^- \rightarrow O^+ + O + 2e^-$ and to a lesser extent photoionization. Also shown is the projected flyby trajectory of Galileo. Figure 1b shows the same distribution in perpendicular cuts on an expanded spatial scale. In both plates the trailing hemisphere is at

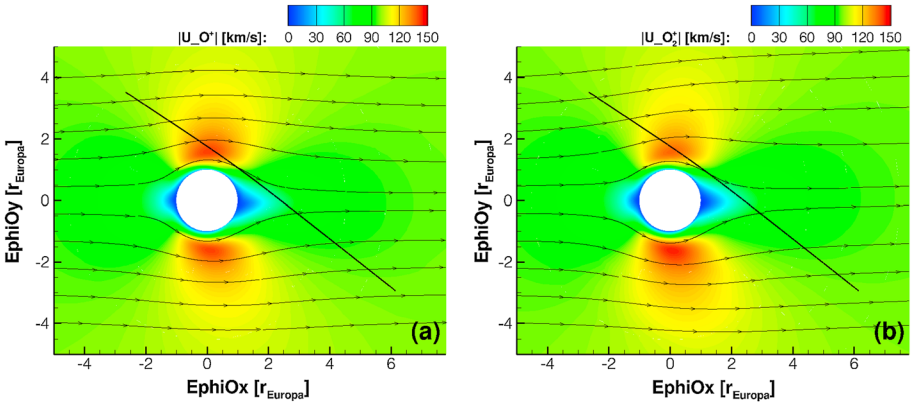

Figure 2. (a) O^+ velocity in the vicinity of Europa for the E4 flyby with plasma streamlines in EphiO coordinates. The black line shows Galileo's trajectory projected onto this plane from roughly 20 min before until 30 min after closest approach. The trailing hemisphere facing the inflow of the magnetospheric plasma is on the left-hand side. The positive EphiO *y* direction points toward Jupiter. (b) The same for the O_2^+ pickup ions.

negative *x*. Figures 1c and 1d show the corresponding distribution of the O_2^+ ions which, in our model, are entirely of pickup origin, together with Galileo's projected flyby trajectory. As discussed in section 2.10 we only include charge exchange for the resonant reaction of O_2 with O_2^+ which yields no net mass loss or addition (terms 2 and 3 of equation (18) cancel each other out) and thus only appears in the momentum equation (equation (19)) and in the pressure source and loss terms (equation (20)) through the exchange of a fast ion by newly implanted slow ion. As can be seen from Figure 1, the ion densities are highest close to the moon where the neutral gas density is highest. From the two plates it becomes obvious that multifluid MHD reproduces asymmetries in the downstream plasma density expected from the physics of the interaction of different plasma populations, i.e., due to the velocity difference between the electrons and the corresponding ion fluid (drift gyration term in equations (2) and (3)): on the trailing hemisphere (upstream side) the plasma density of the magnetospheric population is enhanced on the Jupiter-facing side (positive EphiO y coordinates) while the density of the pickup ions is rather enhanced on the opposite side. Furthermore, on the downstream side the plasma tail is not symmetric and displaced away from Jupiter.

Figure 2 shows the plasma bulk flow streamlines of the two populations with the bulk flow speed in color scale. In some locations the magnetospheric and pickup ions' bulk velocity differs: the two components reach their maximum bulk speeds on the opposite sides of Europa, the O^+ magnetospheric species flow slightly faster on the Jupiter-facing side of the moon while O_2^+ pickup ions reach their maximum velocity on the side facing away from Jupiter. This velocity difference goes into the drift gyration term, which changes sign for ions, moving faster than the electron bulk velocity, calculated from equations (5) and (6), compared to ions moving slower and hence leads to the observed asymmetry in Figure 1. As we have shown in our previous work on comet Halley [*Rubin et al.*, 2014a], although multifluid MHD does not resolve the detailed particle nature of the ion motions, it is able to separate the bulk flows of the fluids in the presence of a magnetic field component along the flow direction, i.e., an $\boldsymbol{E}\times\boldsymbol{B}$ drift, again because it recognizes the velocity difference between electrons and the different ion species [cf. *Rubin et al.*, 2014a]. Also, multifluid MHD is able to reproduce the basic features of an environment with large gyroradii such as around a weak comet [*Rubin et al.*, 2014b]. With the major component of the magnetic field being aligned along the EphiO z direction the dominant component of the drift gyration term is in this plane leading to the asymmetries both on the upstream and downstream sides relative to the direction of the upstream flow.

Figure 3 shows the modeled temperatures of the two plasma components. The left plate shows again the O^+ ions whose temperature is slightly elevated when the plasma approaches Europa due to the implantation of newly created slow ions into the flow and elastic collisions with the neutral gas exosphere. Close to the surface and toward the tail, where the plasma flow is already slowed down significantly, the temperatures also become lower but the lowest temperature, however, is found in the wake. Pickup ions, on the other hand, reach much higher temperatures as can be seen in the plate on the right, and we therefore chose

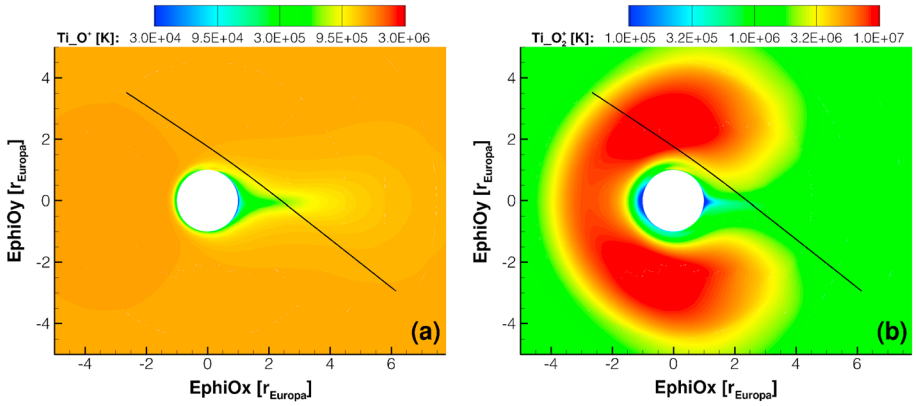

Figure 3. (a) O^+ plasma temperature in the vicinity of Europa for the E4 flyby in EphiO coordinates. The black line shows Galileo's trajectory projected onto this plane from roughly 20 min before until 30 min after closest approach. The trailing hemisphere facing the inflow of the magnetospheric plasma is on the left-hand side. (b) The same for the O_2^+ pickup ions.

different scales for the temperature plots. On the trailing side facing the incoming magnetospheric flow at ~100 km/s (with respect to Europa) the temperatures are increased through addition of new ions to the plasma (initially at rest with respect to the satellite) and through collisional interactions including charge exchange of the plasma with the neutral gas. When the flow is dominated by locally picked-up cold plasma the temperature drops again as the plasma moves down into the tail. The temperature enhancement is particularly pronounced on the flanks where the plasma velocity is highest and the mass loading via electron impact and photoionization contributes ions at very low velocities to the fast magnetospheric flow and, to a lesser extent, also ion-neutral reactions lead to an increase in plasma temperature. Consistent with Figure 2 there is also a slight asymmetry in the modeled temperature between the positive and negative *y* directions, i.e., the temperature is slightly higher on the flank with the higher plasma velocity on the side facing away from Jupiter.

Figure 4a shows an overview of the electron temperature, which is crucial for calculating the electron impact ionization rate. The impacting electron has to provide the ionization energy, and furthermore an additional cold electron is created. Therefore, in regions of increased mass loading, i.e., close to the Europa, the electron temperature drops until a steady state situation is reached. The electron temperature then increases again slowly in the wake, enhanced by the electron heat conduction along the magnetic field lines. Figure 4b shows contours of the magnetic field strength. The magnetic field is a combination of the induced dipolar field, which is located in this plane (17° eastern longitude from the Jupiter-facing meridian), together with the mass loading signature superimposed on the undisturbed upstream magnetic field.

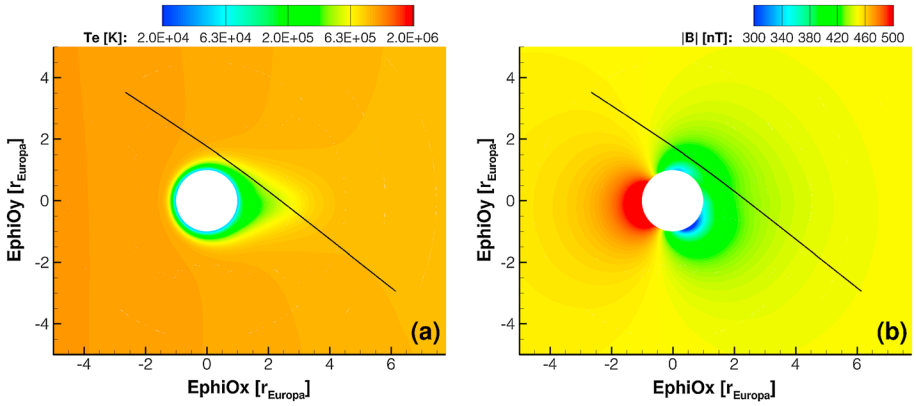

Figure 4. (a) Electron temperature and (b) magnetic field strength in the vicinity of Europa for the E4 flyby. The black line shows Galileo's trajectory projected onto this plane from roughly 20 min before until 30 min after closest approach. The trailing hemisphere facing the inflow of the magnetospheric plasma is on the left-hand side.

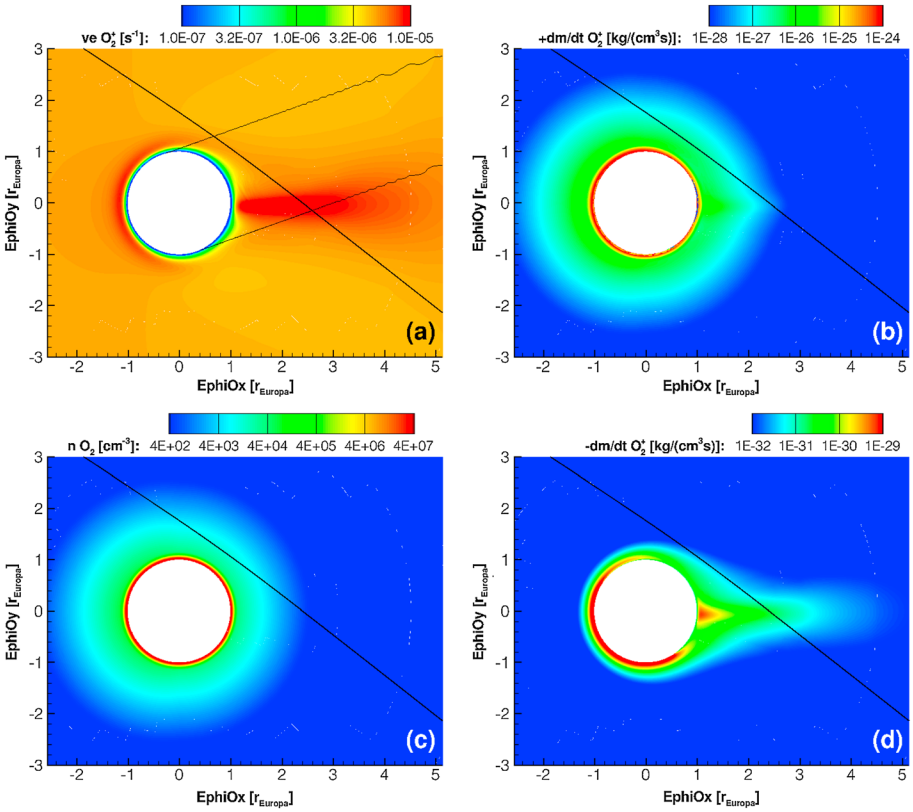

Figure 5. (a) Electron impact ionization frequency for the branch of O_2^+ from neutral O_2 derived from the electron temperature (Figure 4) and the electron density (equation (23) multiplied by the electron number density from equation (5)). The two thin lines indicate the edge of the shadow cast by Europa (no photoionization). (b) O_2^+ mass loading rate near Europa (in kg/(cm^3 s)) derived from the product of the electron impact ionization frequency (Figure 5a) and (c) the neutral gas density based on equation (22). (d) Mass loss rate due to O_2^+-electron recombination (in kg/(cm^3 s)) derived from the ion density (Figure 1) and the electron temperature through equation (24). The trailing hemisphere facing the inflow of the magnetospheric plasma is on the left-hand side. The black line shows Galileo's trajectory of the E4 flyby projected onto this plane.

The local neutral gas density and the electron temperature and density govern the mass loading, however, the major ionization source, which is electron impact ionization, also draws energy from the electrons until a steady state is reached in our model. The electron impact ionization frequency is not a free parameter while the neutral gas distribution was held constant during our simulations. Figure 5 shows the distribution of the mass loading in the EphiO *x-y* plane for the O_2^+ pickup ion population. As previously discussed the highest mass loading is located close to the moon. There is also limited mass loading of O^+ ions based on the $O_2 + e^- \rightarrow O^+ + O + 2e^-$ branch for which we estimated the ionization rate to be 10% of the main channel $O_2 + e^- \rightarrow O_2^+ + 2e^-$. The mass loss through ion-electron recombination is very small and located in regions where the ion and electron densities are high and the electron temperatures are low. In places where the electron temperature is high, ion-electron recombination becomes negligible. Therefore, the dominant loss process is the impact of the ions on the surface of the moon, which will be discussed later. The same figure also shows the electron impact ionization frequency, which is a function of the electron temperature and density. The highest rates can be found on the trailing hemisphere. Integrated over the whole domain the mass addition for O_2^+ and O^+ amounts to 5.14 kg/s and 0.27 kg/s, respectively. For comparison *Kabin et al.* [1999] derived 3.75 kg/s in their model run with best fit to Galileo observations.

As implemented in our model the electrons have to provide the ionization energy for the electron impact ionization. In regions of high mass loading the electron temperature decreases until electron impact ionization subsides (cf. equation (23)). Therefore, a higher neutral density does not increase the mass

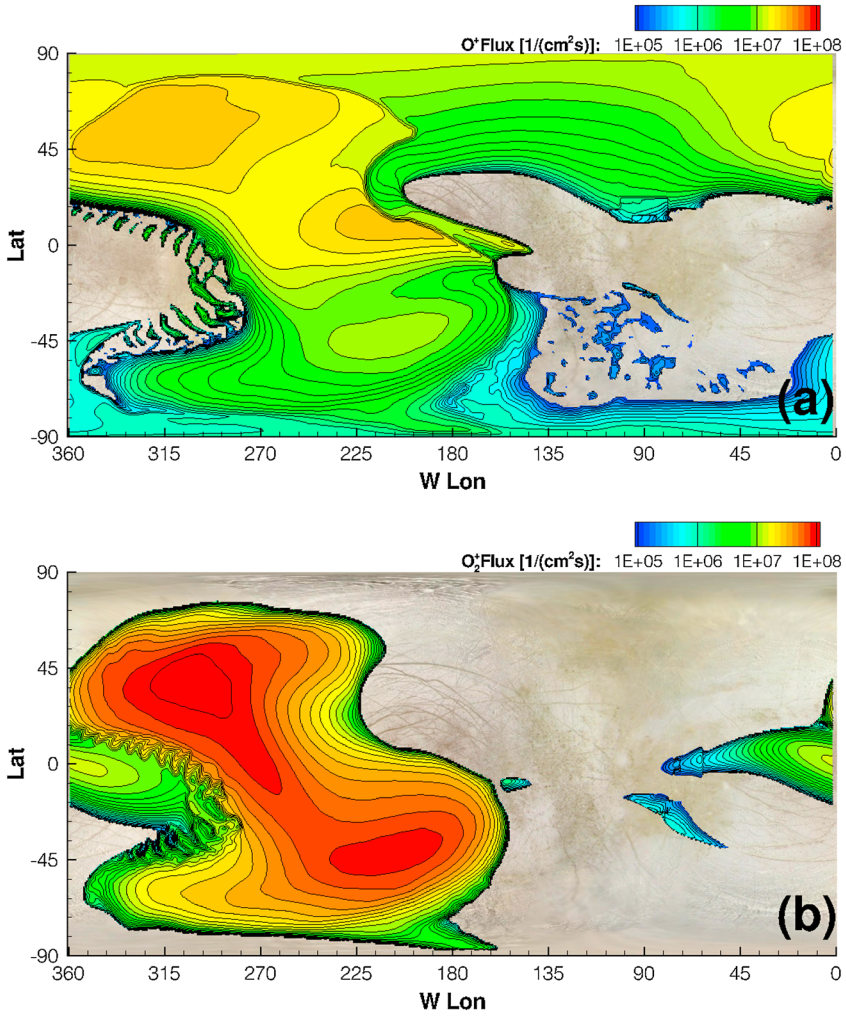

Figure 6. (a) Magnetospheric O^+ and (b) O_2^+ pickup ion fluxes impinging on the surface for the plasma conditions of the E4 flyby (thermal populations). The coordinates are given in west longitude from the Jupiter-facing meridian. The trailing hemisphere is centered at 270° west longitude (cf. 280 nm SO_2 absorption feature on the surface from *Hendrix et al.* [2011]).

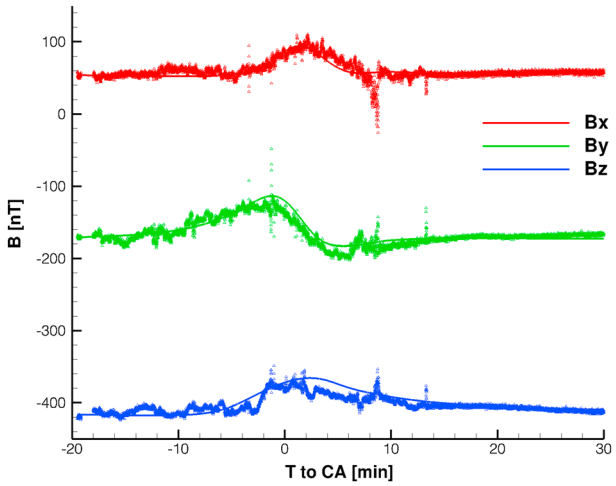

Figure 7. Magnetic field components for the E4 flyby; B_x component on top, B_y in the center, and B_z on the bottom compared to Galileo magnetometer measurements from which the contribution of Jupiter's magnetospheric field has been removed.

loading when the electrons become too cold for efficient electron impact ionization. Obviously, most of the mass loading occurs in regions of high neutral gas density.

The asymmetry between the fluids (O^+ and O_2^+) can be observed in Figure 6 where the ion fluxes impinging on the surface are plotted. Whereas both fluids impact predominantly the trailing hemisphere (centered at 270° west longitude), parts of the pickup ions (Figure 6b) also impact the Jupiter-facing hemisphere (270–360° and 0–90°) (cf. Figure 1), although

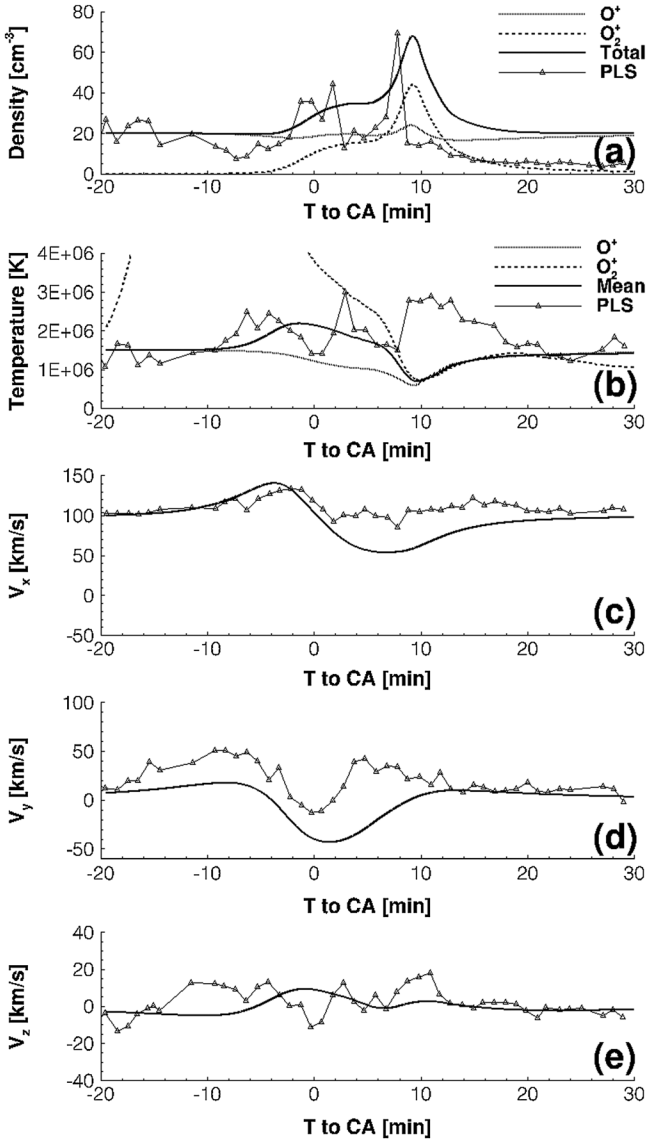

Figure 8. Comparison to the Galileo PLS measurements [*Paterson et al.*, 1999] of the E4 flyby. (a–e): individual modeled ion densities and total density, individual modeled ion temperatures, and number density-averaged temperature, and the three components of the bulk velocity of the thermal plasma population together with the corresponding PLS measurements.

to a lesser extent. For the average impinging ion fluxes over the whole surface we obtained $1.20 \cdot 10^7$ cm^{-2} s^{-1} for O_2^+ and $4.31 \cdot 10^6$ cm^{-2} s^{-1} for O^+, respectively. As stated earlier, impinging ions are responsible for the formation of Europa's thin neutral gas atmosphere. However, to simulate the production of neutral atoms and molecules the MHD approach is not adequate. A model that represents the particle nature of the ions is needed and in particular the effects of high-energy magnetospheric ions need to be taken into account because their sputtering yield can be orders of magnitude larger than those of the thermal ions. Furthermore, the large gyroradii of high-energy ions allow them to access the leading hemisphere of the moon as well as the trailing hemisphere. Nevertheless, the plot shows where the thermal bulk plasma hits the surface. Although we use atomic oxygen ions in our simulations, the magnetospheric plasma population also contains sulfur ions. *Hendrix et al.* [2011] showed the distribution of the 280 nm SO_2 absorption feature on Europa's surface, possibly originating from the deposition of sulfur in the ice of the trailing hemisphere. As expected also in our model the highest fluxes of magnetospheric ions are on the trailing hemisphere.

The magnetic field obtained with our model for the E4 flyby is shown in Figure 7 as a function of the time with respect to the closest approach (CA) in units of minutes. It should be noted that since we run our model using a steady state approach we assumed conditions at closest approach and kept both Jupiter's magnetic field and the induced dipolar field constant throughout the simulation. *Kabin et al.* [1999] required a rotated magnetospheric inflow direction by 20° to match the magnetic field of Galileo's E4 flyby at the moon. Our model, however, seems to reproduce the magnetic field observations quite well for an unaltered inflow direction. Along the Galileo trajectory, the perturbations in the B_x and B_y components are dominated by the induced magnetic field (see Table 2), while the perturbation in the B_z component is governed primarily by the mass loading process.

Distributions of the thermal and pickup ions at Europa were measured by the PLasma Subsystem (PLS) [*Frank et al.*, 1992] and the corresponding moments are presented in *Paterson et al.* [1999]. Figure 8 shows the modeled plasma parameters along the flyby trajectory. The ion densities are shown in Figure 8a, separately for the individual species modeled, their sum, and the total measured density. The O_2^+ population dominates the ion

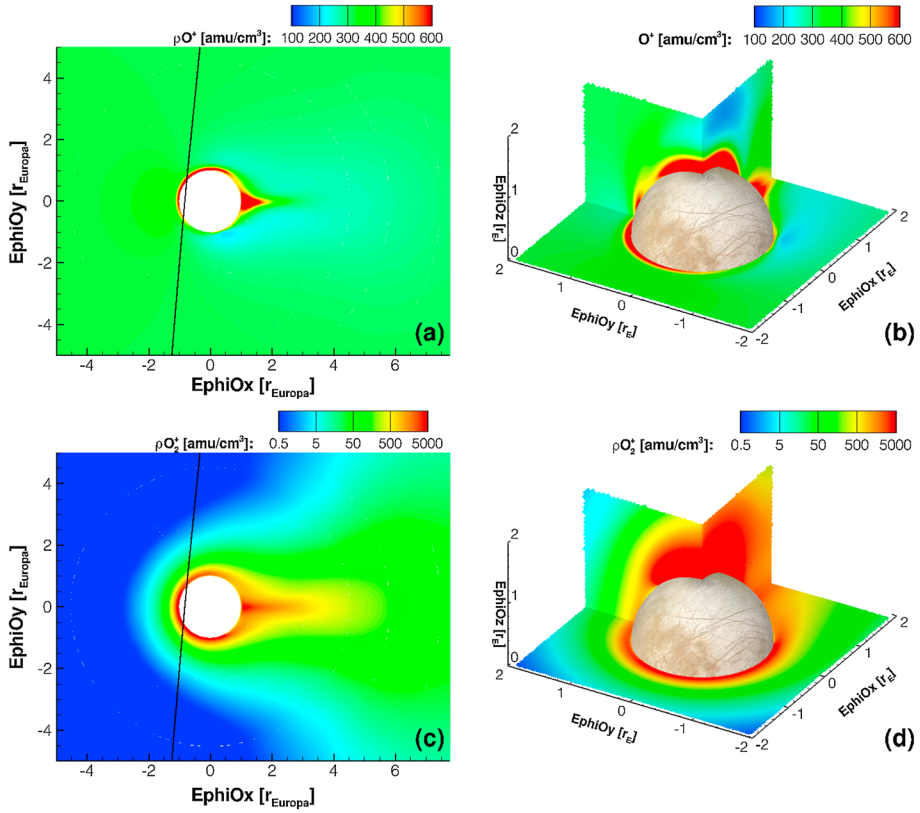

Figure 9. (a) O^+ mass density around Europa for the E26 flyby in EphiO coordinates in the *x-y* plane. The trailing hemisphere facing the inflow of the magnetospheric plasma is on the left-hand side. The black line shows Galileo's trajectory projected onto this plane. The positive EphiO *y* direction points toward Jupiter. (b) The near-Europa environment with three cuts. (c, d) Same as Figures 9a and 9b but for O_2^+.

density inside the wake, whereas the magnetospheric population dominates at larger distances from the moon. *Gurnett et al.* [1998] presented electron number densities obtained from the Galileo plasma wave instrument. Since our model assumes singly charged ions and charge neutrality, we are underestimating the number of electrons in Europa's environment by roughly 50–100% while more or less matching the total ion densities. We plot Galileo plasma science (PLS) plasma densities in the figure for comparison [*Paterson et al.*, 1999]. Galileo PLS observed two peaks, one at closest approach and one when passing through the wake. While our model does not yield a wake as narrow as observed, we do see the double-peak structure in plasma density and the locations of those peaks are close to where the measured peaks fall.

The electron densities we obtained at Europa's surface in our model were roughly a factor of 10 lower than those inferred from radio occultation observations [*Kliore et al.*, 1997]. Up to a factor 2 could potentially be explained by the fact that we assume only singly charged ions in our model as discussed above. There still remains a discrepancy of a factor 5, most probably because in our model the electron temperature drops considerably close to the surface, which in turn reduces the electron impact ionization rate and thus the production of new electrons. However, even in the measurements themselves there are significant differences. A comparison at the closest approach during the E4 flyby at roughly 700 km above the surface (~1.45 R_E from the center) reveals an electron density of approximately 4000 cm^{-3} from the radio occultation observations [*Kliore et al.*, 1997] while an ion density of roughly 40 cm^{-3} (cf. Figure 8) was derived from PLS measurements [*Paterson et al.*, 1999] and the plasma wave instrument observations [*Gurnett et al.*, 1998] yielded an electron density in the 100 cm^{-3} range. One reason could be the model used by *Kliore et al.* [1997] to turn the line of sight electron column densities into a number density profile along the flyby path. Furthermore, also temporal variations could be of importance and variations in the solar radiation, however, this is beyond the scope of this work.

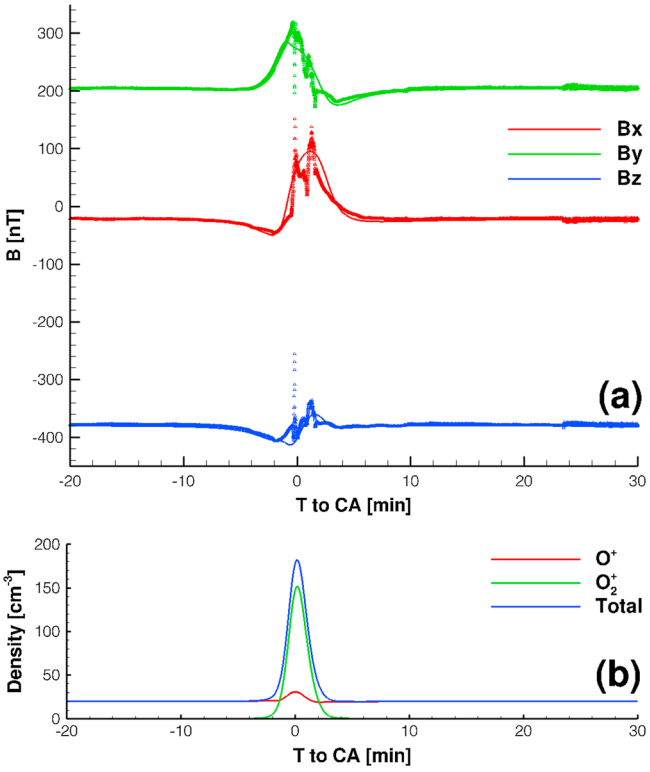

Figure 10. (a) Magnetic field components for the E26 flyby; B_x component on top, B_y in the center, and B_z on the bottom compared to Galileo magnetometer measurements for which the time-dependent contribution due to the rotation of Jupiter's magnetosphere has been removed. (b) Modeled plasma densities along the Galileo flyby trajectory for the two plasma components.

Figure 8b shows the modeled temperature of the two ion components, individually, and the number density-averaged temperature for comparison to the PLS measurements [*Paterson et al.*, 1999]. For visibility we have limited the temperature scale of the pickup ions in regions of low mass loading: our model suggests a maximum temperature along the Galileo trajectory of the pickup ion population of roughly 10^7 K. Figures 8c–8e show the three components of the thermal plasma bulk velocity. The model reproduces the general characteristics of the wake structure of the moon although some properties are not well modeled, especially the temperature. It is clear that our results should be understood within the limitations of the MHD approach. Even though the gyroradii of the thermal ions are rather small compared to the magnetospheric scales of interest [*Lipatov et al.*, 2013], an MHD simulation is less accurate than a hybrid approach for modeling details of a pickup ion distribution [*Lipatov et al.*, 2010].

4.2. Simulation Results for the E26 Flyby and Comparison to E4

The model has also been applied to Galileo's E26 flyby of the moon. As contrasted with the E4 flyby, the pass occurred in the upstream portion of Europa's orbit below the orbital plane of the moon (negative EphiO z direction at a distance of 1.22 R_E from the center of the moon). The model input parameters can be found

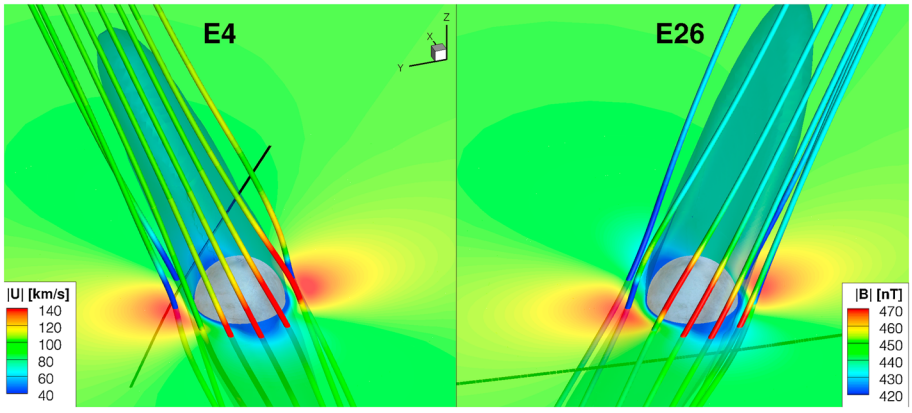

Figure 11. Alfvén wing structure for both flybys. The $z = 0$ cut gives the mass-averaged plasma velocity and the shown isosurface corresponds to a velocity of 50 km/s. The magnetic field lines are color coded with the magnetic field strength. The undisturbed plasma flow is along the x axis and the direction to Jupiter in the direction of y. The corresponding flyby trajectories, which are partially (E4) or fully (E26) at negative z coordinates, are indicated in black. The color scales and orientation are the same for both plates.

in Table 2. We used the same neutral gas model distribution for both flybys; however, the two encounters with Europa occurred at different locations with respect to Jupiter's plasma sheet, and therefore, the upstream magnetic field and the induced dipole field differ between the two cases. Given that the rest of the model parameters (e.g., plasma conditions and Europa's atmospheric conditions) are still quite similar, we show only a selected set of figures. Figure 9 shows the mass densities of both species together with the projected flyby trajectory, and Figure 10 compares the obtained magnetic field with the Galileo magnetometer measurements. Also, the number densities of both populations have been extracted along the flyby path and are plotted in the bottom plate of the figure. The perturbation to the Jovian background field in the z component is slightly shifted in our model. Nevertheless, in general, the model seems to match the observations on the E26 flyby reasonably well.

The Alfvén wing structure at the times of both the E4 and E26 flybys of Galileo are shown in Figure 11. The passes took place with Europa being at different locations with respect to Jupiter's central plasma sheet and therefore encountered distinct upstream magnetic field conditions, i.e., opposite signs of the B_x and B_y components which lead to a change in orientation of the Alfvén wings. The E4 flyby crossed the wake while E26 occurred close to the pole and slightly upstream of Europa.

5. Summary and Conclusions

We have successfully adapted the BATS-R-US multifluid MHD model to simulate the interaction of Europa's plasma environment with Jupiter's magnetosphere. In the present work, we include Jupiter's magnetospheric plasma and the pickup ions originating from Europa's exosphere as two separate ion fluids. The interaction between the fluids leads to asymmetries observable in the corresponding plasma distributions resulting from the separation of pickup and magnetospheric dominated ion populations in our model and their interaction through the fields.

Solving individual pressure equations for the ions and electrons furthermore reveals significant differences to previous single-fluid MHD calculations. The much higher temperature in the pickup ion population compared to the magnetospheric population is expected from the nature of the pickup process: ions are implanted at almost zero velocity in the frame of Europa and reach up to twice the magnetospheric flow velocity during a single gyration. Here in multifluid MHD these particles move on average at the magnetospheric flow velocity and their gyration is represented by a high temperature (thermal velocity ranging from 0 to twice the bulk velocity). Although the fluid model does not track individual particles in their gyration, it does reproduce the high temperature one would derive in a kinetic model.

The self-consistent model of the electron temperature allows computing the local ionization and thus mass loading rate without an a priori choice of ionization rate [*Kabin et al.*, 1999]. Still, the resulting mass loading rates are in accord with these previous simulations: our model suggests a total mass loading rate of 5.41 kg/s for the E4 flyby and 4.99 kg/s for the E26 flyby.

The model is able to reproduce Galileo magnetometer measurements during the E4 [*Kivelson et al.*, 1999] and E26 flybys quite well, while there are still discrepancies with the plasma observations of the PLS instrument [*Paterson et al.*, 1999] during the E4 flyby. Nevertheless, most of the basic structures of the plasma flow in the wake of Europa are reproduced.

As expected the particle fluxes of the thermal populations onto the surface are centered on the trailing hemisphere colocated with the SO_2 absorption feature reported by *Hendrix et al.* [2011]. However, parts of the two populations also impact the surface on the opposite sides of the moon with respect to the Europa-Jupiter line.

In the future we plan to include the diffusion of the magnetic field into Europa. This will be needed to interpret upcoming JUpiter ICy moons Explorer (JUICE) and other Europa-related missions with the goal to characterize the extent of a subsurface brine water ocean.

Acknowledgments
This work has been supported by the Swiss National Science Foundation, NASA Outer Planets Research Program grant NNX12AM74G, NASA Planetary Atmospheres program grant NNX09AB59G, NASA grant NNX13AI66G, and JPL NASA Prime contract NNN12AA01C. The simulations have been performed with the Space Weather Modeling Framework developed at the University of Michigan which is open source and available free of charge after registration. The simulation results are available from the corresponding author (martin.rubin@space.unibe.ch). The authors thank the reviewers for their helpful comments.

Yuming Wang thanks the reviewers for their assistance in evaluating this paper.

References

Bagenal, F. (1994), Empirical model of the Io plasma torus: Voyager measurements, *J. Geophys. Res.*, *99*, 11,043–11,062, doi:10.1029/93JA02908.

Banks, P. M., and G. Kockarts (1973), *Aeronomy Part A*, Academic Press, New York/London.

Brown, M. E., and R. E. Hill (1996), Discovery of an extended sodium atmosphere around Europa, *Nature*, *380*, 229–231.

Cassidy, T., P. Coll, F. Raulin, R. W. Carlson, R. E. Johnson, M. J. Loeffler, K. P. Hand, and R. A. Baragiola (2010), Radiolysis and photolysis of icy satellite surfaces: Experiments and theory, *Space Sci. Rev.*, *153*, 299–315.

Cassidy, T. A., R. E. Johnson, M. A. McGrath, M. C. Wong, and J. F. Cooper (2007), The spatial morphology of Europa's near-surface O_2 atmosphere, *Icarus*, *191*, 755–764.

Cassidy, T. A., R. E. Johnson, P. E. Geissler, and F. Leblanc (2008), Simulation of Na *D* emission near Europa during eclipse, *J. Geophys. Res.*, *113* E02005, doi:10.1029/2007JE002955.

Cassidy, T. A., R. E. Johnson, and O. J. Tucker (2009), Trace constituents of Europa's atmosphere, *Icarus*, *201*, 182–190.

Cooper, J. F., R. E. Johnson, B. H. Mauk, H. B. Garrett, and N. Gehrels (2001), Energetic ion and electron irradiation of the icy galilean satellites, *Icarus*, *149*, 133–159.

Famá, M., J. Shi, and R. A. Baragiola (2008), Sputtering of ice by low-energy ions, *Surf. Sci.*, *602*, 156–161.

Frank, L. A., K. L. Ackerson, J. A. Lee, M. R. English, and G. L. Pickett (1992), The plasma instrumentation for the Galileo mission, *Space Sci. Rev.*, *60*, 283–304.

Glocer, A., G. Tóth, Y. Ma, T. Gombosi, J. C. Zhang, and L. M. Kistler (2009), Multifluid Block-Adaptive-Tree Solar wind Roe-type Upwind Scheme: Magnetospheric composition and dynamics during geomagnetic storms—Initial results, *J. Geophys. Res.*, *114*, A12203, doi:10.1029/2009JA014418.

Gurnett, D. A., W. S. Kurth, A. Roux, S. J. Bolton, E. A. Thomsen, and J. B. Groene (1998), Galileo plasma wave observations near Europa, *Geophys. Res. Lett.*, *25*, 237–240, doi:10.1029/97GL03706.

Hall, D. T., D. F. Strobel, P. D. Feldman, M. A. McGrath, and H. A. Weaver (1995), Detection of an oxygen atmosphere on Jupiter's moon Europa, *Nature*, *373*, 677–679.

Hall, D. T., P. D. Feldman, M. A. McGrath, and D. F. Strobel (1998), The far-ultraviolet oxygen airglow of Europa and Ganymede, *Astrophys. J.*, *499*, 475, doi:10.1086/305604.

Hansen, C. J., D. E. Shemansky, and A. R. Hendrix (2005), Cassini UVIS observations of Europa's oxygen atmosphere and torus, *Icarus*, *176*, 305–315.

Hendrix, A. R., T. A. Cassidy, R. E. Johnson, C. Paranicas, and R. W. Carlson (2011), Europa's disk-resolved ultraviolet spectra: Relationships with plasma flux and surface terrains, *Icarus*, *212*, 736–743.

Huebner, W. F., J. J. Keady, and S. P. Lyon (1992), Solar photo rates for planetary atmospheres and atmospheric pollutants, *Astrophys. Space Sci.*, *195*, 1–289.

Hwang, W., Y.-K. Kim, and M. E. Rudd (1996), New model for electron-impact ionization cross sections of molecules, *J. Chem. Phys.*, *104*, 2956–2966.

Ip, W.-H. (1996), Europa's oxygen exosphere and its magnetospheric interaction, *Icarus*, *120*, 317–325.

Ip, W.-H., D. J. Williams, R. W. McEntire, and B. H. Mauk (1998), Ion sputtering and surface erosion at Europa, *Geophys. Res. Lett.*, *25*, 829–832, doi:10.1029/98GL00472.

Johnson, R. E. (1989), Application of laboratory data to the sputtering of a planetary regolith, *Icarus*, *78*, 206–210.

Johnson, R. E. (1990), *Energetic Charged-Particle Interactions With Atmospheres and Surfaces*, 1st ed., Springer, Berlin, doi:10.1007/978-3-642-48375-2.

Johnson, R. E., R. M. Killen, J. H. Waite, and W. S. Lewis (1998), Europa's surface composition and sputter-produced ionosphere, *Geophys. Res. Lett.*, *25*, 3257–3260, doi:10.1029/98GL02565.

Kabin, K., M. R. Combi, T. I. Gombosi, A. F. Nagy, D. L. DeZeeuw, and K. G. Powell (1999), On Europa's magnetospheric interaction: A MHD simulation of the E4 flyby, *J. Geophys. Res.*, *104*, 19,983–19,992, doi:10.1029/1999JA900263.

Khurana, K. K., M. G. Kivelson, K. P. Hand, and C. T. Russell (2009), Electromagnetic induction from Europa's ocean and the deep interior, in *Europa*, *The Univ. of Arizona Space Sci. Ser.*, edited by R. T. Pappalardo, W. B. McKinnon, and K. K. Khurana, pp. 571, Univ. of Ariz. Press, Tucson, Ariz.

Khurana, K. K., X. Jia, M. G. Kivelson, F. Nimmo, G. Schubert, and C. T. Russell (2011), Evidence of a global magma ocean in Io's interior, *Science*, *332*(6034), 1186–1189, doi:10.1126/science.1201425.

Kivelson, M. G., K. K. Khurana, S. Joy, C. T. Russell, D. J. Southwood, R. J. Walker, and C. Polanskey (1997), Europa's magnetic signature: Report from Galileo's pass on 19 December 1996, *Science*, *276*, 1239–1241.

Kivelson, M. G., K. K. Khurana, D. J. Stevenson, L. Bennett, S. Joy, C. T. Russell, R. J. Walker, C. Zimmer, and C. Polanskey (1999), Europa and Callisto: Induced or intrinsic fields in a periodically varying plasma environment, *J. Geophys. Res.*, *104*, 4609–4626, doi:10.1029/1998JA900095.

Kivelson, M. G., K. K. Khurana, and M. Volwerk (2009), Europa's interaction with the Jovian magnetosphere, in *Europa*, *The Univ. of Arizona Space Sci. Ser.*, edited by R. T. Pappalardo, W. B. McKinnon, and K. K. Khurana, pp. 545, Univ. of Ariz. Press, Tucson, Ariz.

Kliore, A. J., D. P. Hinson, F. M. Flasar, A. F. Nagy, and T. E. Cravens (1997), The ionosphere of Europa from Galileo radio occultations, *Science*, *277*, 355–358.

Lane, A. L., R. M. Nelson, and D. L. Matson (1981), Evidence for sulphur implantation in Europa's UV absorption band, *Nature*, *292*, 38.

Lipatov, A. S., and M. R. Combi (2006), Effects of kinetic processes in shaping Io's global plasma environment: A 3D hybrid model, *Icarus*, *180*, 412–427.

Lipatov, A. S., J. F. Cooper, W. R. Paterson, E. C. Sittler, R. E. Hartle, and D. G. Simpson (2010), Jovian plasma torus interaction with Europa: 3D hybrid kinetic simulation. First results, *Planet. Space Sci.*, *58*, 1681–1691.

Lipatov, A. S., J. F. Cooper, W. R. Paterson, E. C. Sittler Jr., R. E. Hartle, and D. G. Simpson (2013), Jovian plasma torus interaction with Europa. Plasma wake structure and effect of inductive magnetic field: 3D hybrid kinetic simulation, *Planet. Space Sci.*, *77*, 12–24, doi:10.1016/j.pss.2013.01.009.

Liu, Y., A. F. Nagy, K. Kabin, M. R. Combi, D. L. Dezeeuw, T. I. Gombosi, and K. G. Powell (2000), Two-species, 3D, MHD simulation of Europa's interaction with Jupiter's magnetosphere, *Geophys. Res. Lett.*, *27*, 1791–1794, doi:10.1029/1999GL003734.

Ma, Y.-J., et al. (2007), 3D global multi-species Hall-MHD simulation of the Cassini T9 flyby, *Geophys. Res. Lett.*, *34*, L24S10, doi:10.1029/2007GL031627.

McGrath, M. A., E. Lellouch, D. F. Strobel, P. D. Feldman, and R. E. Johnson (2004), Satellite atmospheres, in *Jupiter: The Planet, Satellites and Magnetosphere*, edited by F. Bagenal, T. E. Dowling, and W. B. McKinnon, pp. 457–483, Cambridge Univ., Press, Cambridge, U. K.

Najib, D., A. F. Nagy, G. Tóth, and Y. Ma (2011), Three-dimensional, multifluid, high spatial resolution MHD model studies of the solar wind interaction with Mars, *J. Geophys. Res.*, *116*, A05204, doi:10.1029/2010JA016272.

Ness, N. F., M. H. Acuna, R. P. Lepping, L. F. Burlaga, K. W. Behannon, and F. M. Neubauer (1979), Magnetic field studies at Jupiter by Voyager 1—Preliminary results, *Science*, *204*, 982–987.

Neubauer, F. M. (1998), The sub-Alfvénic interaction of the Galilean satellites with the Jovian magnetosphere, *J. Geophys. Res.*, *103*, 19,843–19,866, doi:10.1029/97JE03370.

Neubauer, F. M. (1999), Alfvén wings and electromagnetic induction in the interiors: Europa and Callisto, *J. Geophys. Res.*, *104*, 28,671–28,684, doi:10.1029/1999JA900217.

Noll, K. S., H. A. Weaver, and A. M. Gonnella (1995), The albedo spectrum of Europa from 2200 Å to 3300 Å, *J. Geophys. Res.*, *100*, 19,057–19,060, doi:10.1029/94JE03294.
Paranicas, C., A. F. Cheng, and D. J. Williams (1998), Inference of Europa's conductance from the Galileo Energetic Particles Detector, *J. Geophys. Res.*, *103*, 15,001–15,008, doi:10.1029/98JA00961.
Paranicas, C., R. W. Carlson, and R. E. Johnson (2001), Electron bombardment of Europa, *Geophys. Res. Lett.*, *28*, 673–676, doi:10.1029/2000GL012320.
Paranicas, C., J. M. Ratliff, B. H. Mauk, C. Cohen, and R. E. Johnson (2002), The ion environment near Europa and its role in surface energetics, *Geophys. Res. Lett.*, *29*(5), 1074, doi:10.1029/2001GL014127.
Paranicas, C., J. F. Cooper, H. B. Garrett, R. E. Johnson, and S. J. Sturner (2009), Europa's radiation environment and its effects on the surface, in *Europa*, *The Univ. of Arizona Space Sci. Ser.*, edited by R. T. Pappalardo, W. B. McKinnon, and K. K. Khurana, pp. 529, Univ. of Ariz. Press, Tucson, Ariz.
Paterson, W. R., L. A. Frank, and K. L. Ackerson (1999), Galileo plasma observations at Europa: Ion energy spectra and moments, *J. Geophys. Res.*, *104*, 22,779–22,792, doi:10.1029/1999JA900191.
Plainaki, C., A. Milillo, A. Mura, S. Orsini, and T. Cassidy (2010), Neutral particle release from Europa's surface, *Icarus*, *210*, 385–395.
Plainaki, C., A. Milillo, A. Mura, S. Orsini, S. Massetti, and T. Cassidy (2012), The role of sputtering and radiolysis in the generation of Europa exosphere, *Icarus*, *218*, 956–966.
Pospieszalska, M. K., and R. E. Johnson (1989), Magnetospheric ion bombardment profiles of satellites—Europa and Dione, *Icarus*, *78*, 1–13.
Powell, K. G., P. L. Roe, T. J. Linde, T. I. Gombosi, and D. L. de Zeeuw (1999), A solution-adaptive upwind scheme for ideal magnetohydrodynamics, *J. Comput. Phys.*, *154*, 284–309.
Roth, L., J. Saur, K. D. Retherford, D. F. Strobel, P. D. Feldman, M. A. McGrath, and F. Nimmo (2014), Transient water vapor at Europa's South Pole, *Science*, *343*(6167), 171–174.
Rubin, M., M. R. Combi, L. K. S. Daldorff, T. I. Gombosi, K. C. Hansen, Y. Shou, V. M. Tenishev, G. Toth, B. van der Holst, and K. Altwegg (2014a), Comet 1P/Halley multifluid MHD model for the Giotto fly-by, *Astrophys. J. Lett.*, *781*(2), 86–98, doi:10.1088/0004-637x/781/2/86.
Rubin, M., et al. (2014b), Plasma environment of a weak comet—Predictions for Comet 67P/Churyumov–Gerasimenko from multifluid-MHD and Hybrid models, *Icarus*, *242*, 38–49, doi:10.1016/j.icarus.2014.07.021.
Rusanov, V. V. (1961), Calculation of interaction of non-steady shock waves with obstacles, *J. Comput. Math. Phys.*, *1*, 267.
Saad, Y., and M. H. Schultz (1986), GMRES: A generalized minimal residual algorithm for solving nonsymmetric linear systems, *SIAM J. Sci. Stat. Comput.*, *7*(3), 856–869, doi:10.1137/0907058.
Samson, J. A. R., and J. L. Gardner (1975), On the ionization potential of molecular oxygen, *Can. J. Phys.*, *53*(19), 1948–1952, doi:10.1139/p75-244.
Saur, J., D. F. Strobel, and F. M. Neubauer (1998), Interaction of the Jovian magnetosphere with Europa: Constraints on the neutral atmosphere, *J. Geophys. Res.*, *103*, 19,947–19,962, doi:10.1029/97JE03556.
Saur, J., P. D. Feldman, L. Roth, F. Nimmo, D. F. Strobel, K. D. Retherford, M. A. McGrath, N. Schilling, J.-C. Gérard, and D. Grodent (2011), Hubble Space Telescope/Advanced Camera for surveys observations of Europa's atmospheric ultraviolet emission at eastern elongation, *Astrophys. J.*, *738*, 153.
Schilling, N. (2006), Time varying interaction of Europa's atmosphere–ionosphere and it's conducting ocean with the Jovian magnetosphere, PhD thesis, Univ. of Cologne.
Schilling, N., F. M. Neubauer, and J. Saur (2008), Influence of the internally induced magnetic field on the plasma interaction of Europa, *J. Geophys. Res.*, *113*, A03203, doi:10.1029/2007JA012842.
Schreier, R., A. Eviatar, V. M. Vasyliunas, and J. D. Richardson (1993), Modeling the Europa plasma torus, *J. Geophys. Res.*, *98*, 21,231–21,243, doi:10.1029/93JA02585.
Schunk, R., and A. Nagy (2009), *Ionospheres: Physics, Plasma Physics, and Chemistry*, Cambridge Univ. Press, Cambridge, U. K.
Shematovich, V. I., R. E. Johnson, J. F. Cooper, and M. C. Wong (2005), Surface-bounded atmosphere of Europa, *Icarus*, *173*, 480–498.
Shi, M., R. A. Baragiola, D. E. Grosjean, R. E. Johnson, S. Jurac, and J. Schou (1995), Sputtering of water ice surfaces and the production of extended neutral atmospheres, *J. Geophys. Res.*, *100*(E12), 26,387–26,395, doi:10.1029/95JE03099.
Smyth, W. H., and M. L. Marconi (2006), Europa's atmosphere, gas tori, and magnetospheric implications, *Icarus*, *181*, 510–526.
Spencer, J. R., L. K. Tamppari, T. Z. Martin, and L. D. Travis (1999), Temperatures on Europa from Galileo photopolarimeter-radiometer: Nighttime thermal anomalies, *Science*, *284*, 1514–1516.
Tóth, G., et al. (2005), Space Weather Modeling Framework: A new tool for the space science community, *J. Geophys. Res.*, *110*, A12226, doi:10.1029/2005JA011126.
Tóth, G., et al. (2012), Adaptive numerical algorithms in space weather modeling, *J. Comput. Phys.*, *231*(3), 870–903, doi:10.1016/j.jcp.2011.02.006.
Truscott, P., D. Heynderickx, A. Sicard-Piet, and S. Bourdarie (2011), Simulation of the radiation environment near Europa using the geant4-based PLANETOCOSMICS-J model, *IEEE Trans. Nucl. Sci.*, *58*, 2776–2784.
van der Holst, B., et al. (2011), CRASH: A Block-adaptive-mesh Code for Radiative Shock Hydrodynamics—Implementation and verification, *Astrophys. J. Supp.*, *194*(2), 23.
van der Holst, B., I. V. Sokolov, X. Meng, M. Jin, W. B. Manchester, G. Tóth, and T. I. Gombosi (2014), Alfvén wave solar model (AWSoM): Coronal heating, *Astrophys. J. Lett.*, *782*(2), 81.
Volwerk, M., M. G. Kivelson, and K. K. Khurana (2001), Wave activity in Europa's wake: Implications for ion pickup, *J. Geophys. Res.*, *106*, 26,033–26,048, doi:10.1029/2000JA000347.
Volwerk, M., K. Khurana, and M. Kivelson (2007), Europa's Alfvén wing: Shrinkage and displacement influenced by an induced magnetic field, *Ann. Geophys.*, *25*, 905–914.
Williams, D. J., R. W. McEntire, S. Jaskulek, and B. Wilken (1992), The Galileo energetic particles detector, *Space Sci. Rev.*, *60*, 385–412.
Wolff, R. S., and D. A. Mendis (1983), On the nature of the interaction of the Jovian magnetosphere with the icy Galilean satellites, *J. Geophys. Res.*, *88*, 4749–4769, doi:10.1029/JA088iA06p04749.
Zimmer, C., K. K. Khurana, and M. G. Kivelson (2000), Subsurface oceans on Europa and Callisto: Constraints from Galileo magnetometer observations, *Icarus*, *147*, 329–347.

Erratum

In the originally published version of this article, there were errors in equations (18) and (19). The equations have since been corrected, and this version may be considered the authoritative version of record.